



Collective dynamics in entangled worm and robot blobs

Yasemin Ozkan-Aydin^a, Daniel I. Goldman^a, and M. Saad Bhamla^{b,1}

^aSchool of Physics, Georgia Institute of Technology, Atlanta, GA 30332; and ^bSchool of Chemical and Biomolecular Engineering, Georgia Institute of Technology, Atlanta, GA 30332

Edited by John A. Rogers, Northwestern University, Evanston, IL, and approved December 31, 2020 (received for review May 27, 2020)

Living systems at all scales aggregate in large numbers for a variety of functions including mating, predation, and survival. The majority of such systems consist of unconnected individuals that collectively flock, school, or swarm. However, some aggregations involve physically entangled individuals, which can confer emergent mechanofunctional material properties to the collective. Here, we study in laboratory experiments and rationalize in theoretical and robophysical models the dynamics of physically entangled and motile self-assemblies of 1-cm-long California blackworms (*Lumbriculus variegatus*, Annelida: Clitellata: Lumbriculidae). Thousands of individual worms form braids with their long, slender, and flexible bodies to make a three-dimensional, soft, and shape-shifting “blob.” The blob behaves as a living material capable of mitigating damage and assault from environmental stresses through dynamic shape transformations, including minimizing surface area for survival against desiccation and enabling transport (negative thermotaxis) from hazardous environments (like heat). We specifically focus on the locomotion of the blob to understand how an amorphous entangled ball of worms can break symmetry to move across a substrate. We hypothesize that the collective blob displays rudimentary differentiation of function across itself, which when combined with entanglement dynamics facilitates directed persistent blob locomotion. To test this, we develop a robophysical model of the worm blobs, which displays emergent locomotion in the collective without sophisticated control or programming of any individual robot. The emergent dynamics of the living functional blob and robophysical model can inform the design of additional classes of adaptive mechanofunctional living materials and emergent robotics.

organismal collective | entangled active matter | emergent mechanics | swarming robot | collective behavior

Active matter collectives consists of self-propelled individual units (living or artificial) that interact with each other to gain emergent functionality or to achieve common tasks (1–7). In these systems, repeated interactions between the individuals and their environment can produce complex behaviors at the group level (3, 5). Depending on the type of interactions, collectives can display either fluid-like or solid-like properties (2). Fluid-like behavior is typically observed in unconnected individuals that avoid physical contact such as in flocking birds or schooling fish (5, 8–12). On the other hand, solid-like behavior is a consequence of physical contact between individuals such as in ants or bee self-assemblages (13–15). The latter type of entangled active matter aggregates enables the formation of large mechanically functional structures (bivouacs, rafts, bridges, etc.) that enable new functionalities not accessible to the individual as well as enabling survival benefits to the collective, especially in harsh and adverse environmental conditions in which it is impossible for individuals to survive on their own (16–20).

In engineered systems, the emergent dynamics of active matter collectives have been explored in particles ranging in size from micrometers (active colloids) to centimeters (robots) (21–25). Specifically, for collective swarm robotics, the majority of

past work has focused on mathematical modeling (26–30). These theoretical approaches often fail to adequately capture real-world physical interactions between individual robots, which may critically influence the emergent collective behavior. Experimentally, although swarming systems have been successfully realized to collectively accomplish a common goal (31–33), each individual robot is equipped with costly and sophisticated sensors to leverage some degree of centralized control, which is subject to many limitations including low fault tolerance, scalability problems, and design complexity (31). To overcome these limitations, researchers have proposed decentralized swarms, which eliminates the need for a central control unit, communication between individual agents, and a priori knowledge about the environment (34–36). These decentralized swarm systems have been demonstrated recently using only physical entanglements, either magnetic (35, 37) or geometric (38), that harness physical coupling between simple robots to yield task-oriented collectives capable of emergent functions.

In this study, we investigate worm blobs as an example of an entangled active matter where the long flexible bodies of blackworms (*Lumbriculus variegatus*) form transient links through braiding. The activity of individual worms in a blob enables worms to self-organize and dynamically respond to changing environmental conditions. Depending on the type, history, and gradient of the environmental stimulus (light, temperature, etc.), the blob can respond in a variety of ways. Here, we specifically focus on the evaporation and thermal responses of worm blobs to understand why worms spontaneously aggregate into blobs

Significance

Living organisms form collectives across all scales, enabling biological functions not accessible by individuals alone. In a few cases, the individuals are physically connected to each other, forming an additional class of entangled active matter systems with emergent mechanofunctionalities of the collective. Here, we describe the dynamics of macroscopic aquatic worms that braid their long, soft bodies to form large entangled worm blobs. We discover that the worm blob behaves as a living material to undergo dynamic shape transformations to reduce evaporation or break-symmetry and locomote to safety against thermal stresses. We validate our biological hypotheses in robophysical swarming blobs, which pave the way for additional classes of mechanofunctional active matter systems and collective emergent robotics.

Author contributions: Y.O.-A., D.I.G., and M.S.B. designed research; Y.O.-A. conceived the setups and performed animal and robot experiments; Y.O.-A. derived the model and analyzed data; and Y.O.-A., D.I.G., and M.S.B. wrote the paper.

The authors declare no competing interest.

This article is a PNAS Direct Submission.

Published under the PNAS license.

¹ To whom correspondence may be addressed. Email: saadb@chbe.gatech.edu.

This article contains supporting information online at <https://www.pnas.org/lookup/suppl/doi:10.1073/pnas.2010542118/-/DCSupplemental>.

Published February 5, 2021.

and how they spontaneously move as whole. By developing robo-physical blobs (39, 40) consisting of three-link robots (smarticles) (38), we describe how variation of gaits and mobility of simple individuals in a physically entangled collective can lead to varying levels of locomotive performance, without the need for sophisticated central control.

Results and Discussion

Worm Blob as Complex Material. Under certain environmental conditions (evaporation, cold temperature, etc.) individual worms spontaneously aggregate to form three-dimensional blobs that range from small collectives ($N = 10$ worms) to large macroscopic entangled networks ($N = 50,000$), both in water and in air (Fig. 1 and *Movie S1*). The blobs display non-Newtonian material properties (41) and can flow at long timescales (SI Appendix, Fig. S1D), while retaining shape to short timescale disturbances (SI Appendix, Fig. S1A and C). The underlying material timescale is set by the physical entanglement of the worm bodies through self-braiding (Fig. 1). The blob formation and disintegration are reversible through changes in ambient fluid temperature (SI Appendix, Fig. S1B). Increasing the fluid temperature “melts” the blob (fluid-like phase), while decreasing the temperature leads to a more entangled, solid-like phase (SI Appendix, Fig. S1B). We posit that the underlying principle for this emergent collective phase behavior lies in the changing activity of individual cold-blooded worms in response to external temperature and cooperative effects of active phase domains (41–46). At lower temperatures ($T < 25^\circ\text{C}$), worms are less motile and elongated, while at higher temperatures ($25 < T \leq 30^\circ\text{C}$), they are more active and coiled up, with a peak activity at $T = 30 \pm 2^\circ\text{C}$ (SI Appendix, Fig. S5) (47). Thus, an entangled solid-like blob is observed at lower temperatures through slow-moving, elongated worms, while a disentangled fluid-like aggregate is observed at higher temperatures (SI Appendix, Fig. S2) due to highly active, coiled-up worms, similar to motility-induced phase separations in active matter (46, 48).

Worms in a Blob Survive Longer against Desiccation. Worms are cold-blooded animals and their activities are greatly influenced

by variations in temperature and light intensity of their surroundings (47, 49). Since blackworms naturally inhabit shallow aquatic regions (42–44), we hypothesize that forming a blob provides survival benefit to individual worms by reducing desiccation in air. To test this hypothesis, we expose blobs of different numbers ($N = 1$ to 1,000 worms, 10 replicates per condition) on a dry plate at controlled temperature and humidity (24°C , 48%) and track the projected blob area, A , using time-lapse imaging over a few hours (SI Appendix, Fig. S4 and *Movie S2*). We observe that a single worm ($N = 1$) perishes in less than 1 h, while worms in a blob ($N = 1,000$) are alive even after 10 h (*Movie S2*). Additionally, the blobs are not static. Larger blobs ($N > 20$) undergo exploratory searches for potentially favorable conditions, during which the projected blob area can almost double (40 min, $N = 100$) (Fig. 2A and B and *Movie S2*). This phase is followed by a shrinking mode during which the blobs become increasingly hemispherical to minimize surface area to volume ratio. In contrast, smaller blobs ($N < 20$) monotonically shrink into hemispherical structures (Fig. 2B). We note that this dynamic shape transformation behavior of worm blobs is reversible: Once the blob has shrunk into a spherical shape, addition of water restarts the search mode (*Movie S2*).

To support the hypothesis that the worm blobs reduce evaporative losses through surface area minimization, we quantify the steady-state projected surface area (A_s , defined as the projected surface area is invariant, i.e., $dA/dt < 1\%$) as a function of blob size N as shown in Fig. 2C and D. Theoretically, we estimate the volume of N worms as $V_w = N \times (\pi r_w^2 h)$, where each worm is assumed to have a cylindrical body of radius r_w and length h . If these N worms minimized surface area by bending and coiling to form a hemisphere, then the theoretical projected surface area of the hemisphere (i.e., area of the circle) is given by $A_{s,\text{th}} = \pi r_b^2$, where $r_b = \sqrt[3]{\frac{3V_w}{4\pi}}$ is the equivalent blob radius. Note that, since the worms have a hydrostatic skeleton, the radius of worms (r_w) decreases with evaporation from their nominal value 0.6 ± 0.1 to 0.3 ± 0.1 mm (SI Appendix, Fig. S7). Indeed, the experimental data and theoretical model are in good agreement over three orders of blob size N between the ranges of evaporated worm

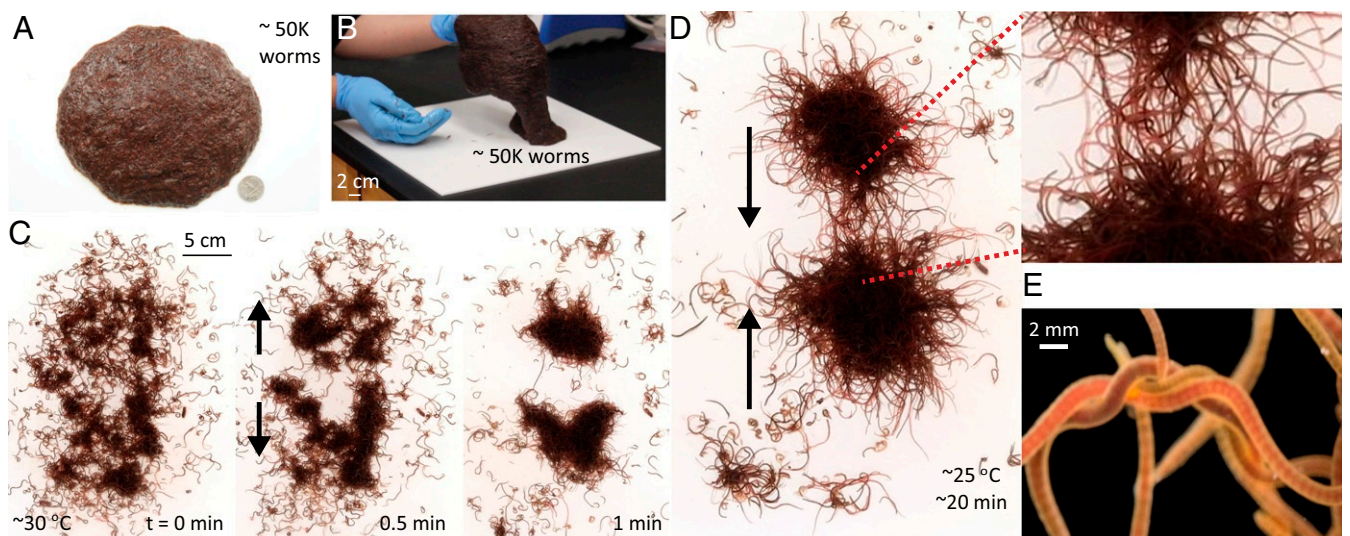


Fig. 1. Worm blobs form via physical entanglements. (A) An entangled worm blob composed of $\sim 50,000$ worms. (B) The worm blob behaves as a non-Newtonian fluid, which can flow at long timescales and maintain shape as a solid at short timescales (*Movie S1*). (C and D) Blob formation in water. The experiment starts in water at $\sim 30^\circ\text{C}$ in which the worms are mainly untangled with each other. As the water cools down to 25°C , the worms aggregate initially into two smaller blobs ($t = 1$ min), which ultimately merge to form one large blob ($t = 20$ min; *Movie S1*). (E) Close view of braid formation within a blob.

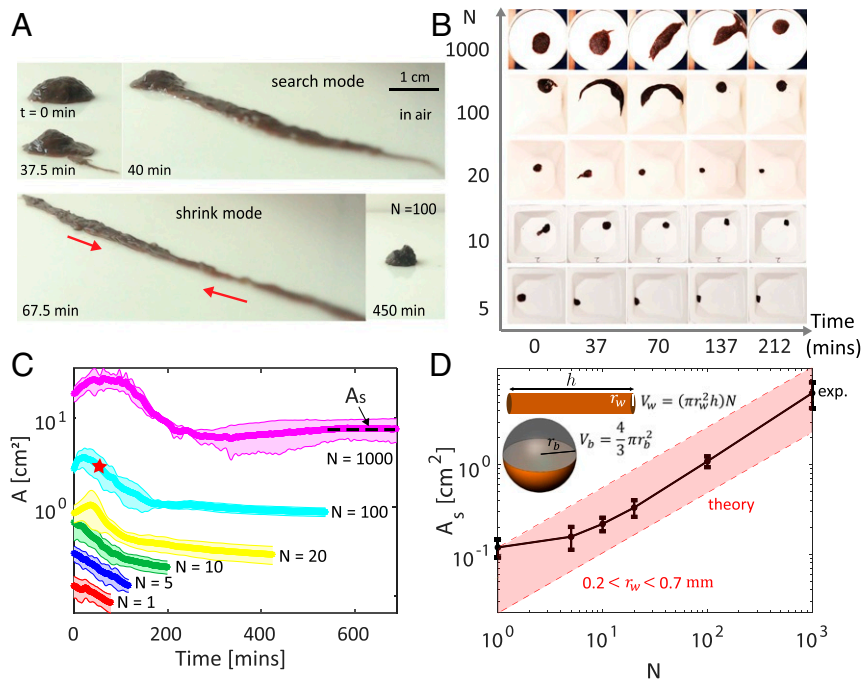


Fig. 2. Water evaporation response of the worm blob. (A) When water is scarce, worms spontaneously form hemispherical blobs as a survival strategy to minimize evaporative losses. Shown is a time snapshot from the experiment (side view, $N = 100$ worms) for 450 min (Movie S2). The worms first undergo a stereotypical search mode for a water source and, after a certain time, spontaneously transition into a shrink mode to reduce surface area. (B) The shape changes of the worm blobs in the air as a function of blob size ($N = 5, 10, 20, 100, 1,000$). See Movie S2 for the example experiments with $N = 1$ and $N = 1,000$. (C) Projected surface area (A) as a function of cluster size ($N = 1, 5, 10, 20, 100$, and $1,000$ worms, 10 replicates per condition) under controlled laboratory conditions (24°C , humidity 48%). The red star on the light blue curve indicates the time when the shrink mode starts. The worm blobs achieve a steady-state area (A_s) indicated by a plateau in the curve, where the change in surface area is minimal ($A_s = dA/dt < 1\%$). (D) Comparison of experimental steady-state projected surface area (A_s) (black) with theoretical estimation of surface area (red) across three orders of magnitude of blob size (N) reveals good agreement between model and experiments. V_w and V_b are the total volume of N worms with a cylindrical body and the volume of a sphere shape worm blob, respectively. The final worm radius (r_w) is calculated from experimental measurements (SI Appendix, Fig. S7).

radius, validating the hypothesis that worm blobs form hemispherical shapes to reduce evaporation losses (Fig. 2 C and D). Beyond *L. variegatus*, other annelids that we tested, such as *Lumbricus terrestris* and *Eisenia fetida* (SI Appendix, Fig. S6 and Movie S2), as well as past observations on nematodes (*Caenorhabditis elegans*) (50–54), suggest forming entangled collectives may be a general biological strategy to survive desiccation for extended periods by these organisms in fluctuating arid environments.

Emergent Locomotion of Worm Blobs. Since the worms are sensitive to temperature (as described earlier) as well as light (42, 45), we next investigate the emergent behavior of the worm blobs in response to a combination of light and temperature cues in a custom setup shown in Fig. 3A (SI Appendix, Fig. S8). In laboratory cultures at constant temperature ($\sim 15^\circ\text{C}$), we observe that the worms form tightly entangled blobs at high light intensities and form loose dispersions in the dark. A sudden increase in light intensity results in a rapid blob contraction ($33 \pm 6\%$ reduction, after 15 h in dark) of a short duration ($t < 5$ s; SI Appendix, Fig. S9 and Movie S3), which is expected as individual worms are known to exhibit a rapid contractile escape response to shadows and photic stimulations arising from movements of overhead predators in the water (55). Thus, bright light serves as a cue for worms to aggregate and entangle tightly.

Under room light intensity (~ 400 lux) if we next expose the blob to an approximately linear temperature gradient (see the experimental setup in Fig. 3A), the blob dissipates and worms individually crawl to the cold side (Fig. 3 B, Left column; SI Appendix, Fig. S10; and Movie S3). Without changing the tem-

perature gradient when we increase the light brightness to 5,500 lux, we discover a surprising behavior: Worms collectively move as a blob toward the cold side (negative thermotaxis; Fig. 3 B, Right column; SI Appendix, Fig. S11; and Movie S3). In both cases, the majority of the worms ($>70\%$ for 400 lux and $>90\%$ for 5,500 lux) are successfully able to move toward the colder side, with a similar average speed (0.6 ± 0.1 cm/min, calculated when 70% of worms reach cold side) as shown in Fig. 3C.

To examine whether moving together as a blob vs. moving individually conferred additional benefits, we utilize a quasi-two-dimensional (quasi-2D) experimental apparatus, which facilitates worm tracking (SI Appendix, Fig. S12 A and B). We find that worms crawling individually can move at faster speed to the cold side ($N = 10$, $v_s = 1.2 \pm 0.3$ cm/min) compared to worms in a blob ($N = 80$, $v_b = 0.4 \pm 0.1$ cm/min). However, moving as a blob despite being slow enabled all of the worms to be transported safely to the cold side. Not all worms moved safely when they crawled individually (SI Appendix, Fig. S12C). Thus, for an individual worm, being in a blob confers multiple survival benefits: reduced evaporation when water is scarce and reliable transport to safety when the environmental temperature becomes fatal.

Mechanism of Blob Locomotion. How does an entangled worm blob spontaneously break symmetry and move? We hypothesize that the locomotion of the blob toward the cold side emerges as a consequence of the individual worm response to temperature. To test this hypothesis, we recorded close-up videos of small worm blobs ($N = 20$) while moving under a thermal gradient (Fig. 4A). Using their circular and longitudinal muscles, the worms can apply contractile pulling forces along the length of

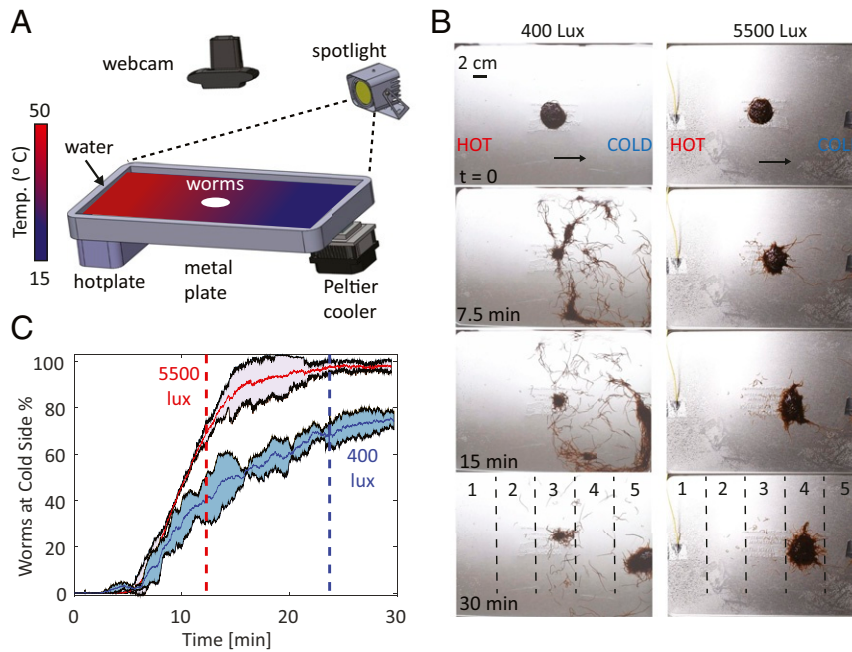


Fig. 3. Worm blobs exhibit emergent locomotion under thermal gradients. (A) Schematic of the experimental setup to study worm blob locomotion under thermal gradients and different light conditions. The worm blob is placed ($N = 600$ worms) into the center of a metal plate ($30 \times 20 \times 5 \text{ cm}^3$) filled with water. We establish thermal gradients on the surface of the plate by setting the temperature of the cold and the hot side to 15°C and 50°C , respectively (see *SI Appendix, Fig. S8* for the details of the setup). Color bar represents the temperature of the water. (B) Time snapshots ($t = 0, 7.5, 15,$ and 30 min) from the thermotaxis navigation experiments under room light (400 lux, *Left*) and spotlight (5,500 lux, *Right*). In both cases, the worms exhibit negative thermotaxis, but under low light intensities, they move individually, while under high light intensities, they move collectively as a blob. Dashed lines divide the plate into five equal areas for tracking movement of worms across the plate. For both experiments, overlap space–time heat maps of worm locomotion are shown in *SI Appendix, Figs. S10 and S11*. (C) During the same duration, by moving together as a blob, $>90\%$ of the worms make it to the colder side (zone 4), while moving individually $>70\%$ of the worms make it to the cold side (zone 5). Dashed lines (red, 5,500 lux; blue, 400 lux) show the time when the same amount of the worms (70%) reach the cold sides in both experiments.

their body to crawl forward (56). As described earlier, the motility (and activity) of the worms increases at higher temperatures (*SI Appendix, Fig. S5*) (47). Thus, depending on the position in a blob (front, rear, or top), individual worms encounter different thermal stimuli. We observe that worms at the top of the blob act as entangling binders to keep the blob as a cohesive unit. Worms facing the cold side (leading edge) act as pullers and use their elongated bodies to apply slow, periodic pulling forces on the blob (*Movie S4* and Fig. 4B and C). The worms closer to the hot side (trailing edge) are more coiled up, lifting up the back of the blob potentially to reduce friction (wigglers, Fig. 4A–C).

To explore this hypothesis further, we first evaluate whether the pulling/wiggling behaviors are correlated with blob displacement. We plot the contraction in length of the puller worms $\Delta L = l(t_f) - l(t_i)$ with the forward displacement of the center of blob, $\Delta x_c = x_c(t_f) - x_c(t_i)$, where t_i and t_f represent the initial and final times (Fig. 4D). Each symbol represents an event where a forward blob movement occurred ($x_c > 1 \text{ mm}$) for a total 17 events from $n = 3$ trials each of $N = 20$ worm blobs (Fig. 4D). We observe that in the majority of the cases (13/17 events), the forward blob displacement Δx is correlated with both a pulling event (negative ΔL due to contraction of puller worms) and vertical lifting of the blob by the wiggler worms (positive y_c). Thus, our data suggest that functional differentiation of worms in a blob into puller worms at the leading edge and friction-reducing worms (wiggling) is a possible mechanism for blob motility. For example, the pull events are visually evident in the accompanying videos (*Movie S4*) as well as in jumps in blob displacement during locomotion of small blobs ($N = 20$) across a substrate (Fig. 4E).

However, since each worm can individually exhibit a wide array of dynamic locomotor behaviors (42, 45, 47), the col-

lective blob locomotion may not be limited to just a binary gait differentiation; more complex mechanisms and emergent cooperative behaviors that build upon this motif are possible. For example, in Fig. 4D there are a few points (4/17) where although the leading puller worms did not contract (positive ΔL), the blob still exhibits significant forward displacement. A closer look at one of these events (point 4 in Fig. 4D) reveals that a few puller worms intertwine to form a braided chain and collectively pull together (*Movie S6*). Moreover, as the blobs become larger ($N > 300$), we observe that the blob moves at a slower speed compared to smaller blobs ($N = 20$), but the movement becomes more consistent compared to the relatively jerky pull events observed in smaller blobs (Fig. 4E). Visualizing the exact behavior (puller vs. wiggler) in these larger blobs is challenging due to the opacity and three-dimensional entanglement in these blobs (*Movie S4*). Thus, although we propose and provide evidence below (using robotic blobs) for a simplistic mechanism for blob motility through gait differentiation by the puller and wiggler worms, we believe that more complex behaviors are possible and yet to be discovered that may further depend on the blob size, external stimulus, and substrate properties.

To support our proposed basic mechanism and test whether a single worm can indeed generate the necessary force to pull a blob, we tether individual worms to a calibrated cantilever beam and measure the pulling force exerted by a single worm on a rigid peg (Fig. 4F and *SI Appendix, Fig. S13*). At low temperatures (20°C), the worms are more elongated and use their bodies to exert large pulling forces ($F_p = 178.2 \pm 52.5 \mu\text{N}$, ~ 2.5 times the weight of a single worm). While at high temperatures (30°C) the forces were nominal $F_p = 28.0 \pm 10.9 \mu\text{N}$ (Fig. 4G and H).

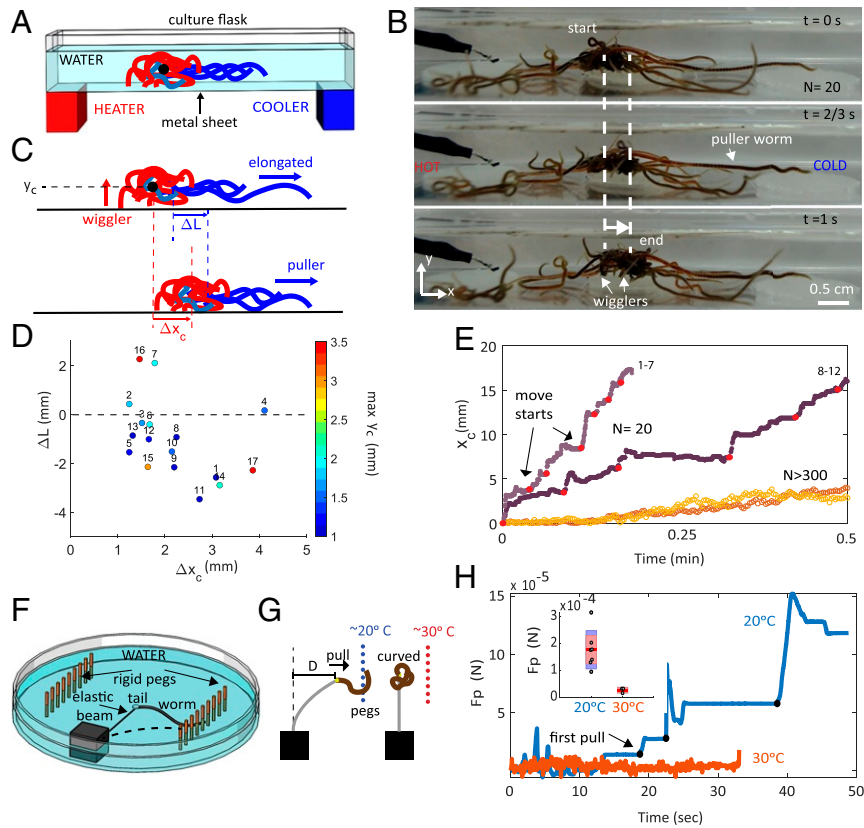


Fig. 4. Mechanism of emergent locomotion of a worm blob through differentiation of activity. (A) Schematic of the experimental setup with enforced temperature gradient. The black dot shows the center of blob (CoB). (B) Snapshots from the quasi-2D experiment, where a small worm blob ($N = 20$) exhibits negative thermotaxis, crawling toward the cold side (Right) in response to a temperature gradient (Movie S4). (C) Proposed mechanism of how an entangled worm blob breaks symmetry to exhibit directed motion. The worm blob moves through differentiation of activity: Worms at the leading edge (blue) act as pullers, while worms at the trailing edge (red) curl up and lift the blob to potentially reduce friction. ΔL is the contraction amount of leading worms and Δx_c is the forward displacement of a worm blob. (D) Correlation plot of changes in the length of the leading-edge puller worms, $\Delta L = l(t_f) - l(t_i)$, and the blob's forward displacement, $\Delta x_c = x_c(t_f) - x_c(t_i)$, where t_i and t_f represents the initial and final times of the peak forward movement (total 17 events from $N = 3$ trials). Color represents the maximum height of the blob ($\max y_c$) during the forward displacement. (E) Horizontal displacement of the center of blob for $N = 20$ (dark and light purple) and $N > 300$ (dark and light yellow) in response to thermal gradients. Red dots on the $N = 20$ case indicate where the pulling events begin (the events [1–7] and [8–12] are shown in D) (Movie S4). (F) Schematic of the experimental setup to measure pulling force of individual worms. The pegs are mounted on a plastic petri dish (100×15 mm) and the tail of the worm is glued to a force-calibrated elastic beam (SI Appendix, Fig. S13). By measuring the deflection of the beam by the worms, pulling force is estimated. (G) Illustration describing the observed behavior during measurements at 20°C (blue) and 30°C (red) as shown in Movie S4. (H) Force measurements for single worms in cold (20°C , blue) and hot water (30°C , red). The black dots on the blue curve indicate the start time of successive pulling events by worms as seen in Movie S4. Inset shows the mean and standard deviation of the maximum pulling forces in cold (five trials) and hot water (three trials).

At higher temperatures, we hypothesize that the worms cannot apply enough force to pull the pegs due to rapid body movements and gait reversal at elevated temperatures (47). Assuming a low coefficient of static friction for wet acrylic ($\mu_s = 0.3$, substrate used in our experiments) and a blob mass of $m = 0.14$ g ($N = 20$ worms), we estimate two to three individual worms could generate sufficient traction force ($F = \mu_s mg = 412$ μN) to move a small blob under certain conditions (low friction, existence of a rigid object to grab and pull the body, etc.). This estimate qualitatively agrees with experimental observations, where individual worms are capable of moving the small blob (Fig. 4C and Movie S4). Taken together, we posit that the locomotion in small blobs can emerge through differential activities of the individuals in the front (puller) and rear (wiggler).

Phototactic Robophysical Blobs. Here we develop an active physical model (a “robophysical” model) (39, 40) of the worm blob to validate our hypothesis that an entangled robotic collective can exhibit emergent locomotion through two central principles: mechanical interactions (entanglements) and function (gait) dif-

ferentiation. The advantage of a robophysical model is that it enables us to examine critical parameters that cannot easily be observed in the biological system and serves as a laboratory platform for testing the individual–environment interactions that could lead to real-world swarming robot collectives.

The robophysical blobs consist of six three-link, two-revolute joints, with planar, smart, active particles (smarticles) (38) equipped with two light sensors as shown in Fig. 5A. Based on the light intensity sensed by these optical sensors, we program robots with three autonomous behaviors as a function of their arm angles α_1 and α_2 (Fig. 5B and Movie S5): 1) For low light intensity (<200 lux), robots execute a wiggler gait, where $\{\alpha_1, \alpha_2\} = [(-\pi/4, -\pi/4), (\pi/4, \pi/4)]$ such that the robot arms swing up and down (out of phase with each other) 45° from the centerline of the body (Fig. 5D). 2) For high light intensity (>800 lux), robots follow a crawler gait, where α_1 and α_2 follow a sequence as shown in Fig. 5B. 3) For intermediate light (200 to 800 lux), robots can either hold their arms straight (rigid) with $\alpha_{1,2} = 0$ or let their arms freely move (flexible) and deform based on neighboring interactions. We note that only the crawler gait leads to forward motion (symmetry breaking) toward

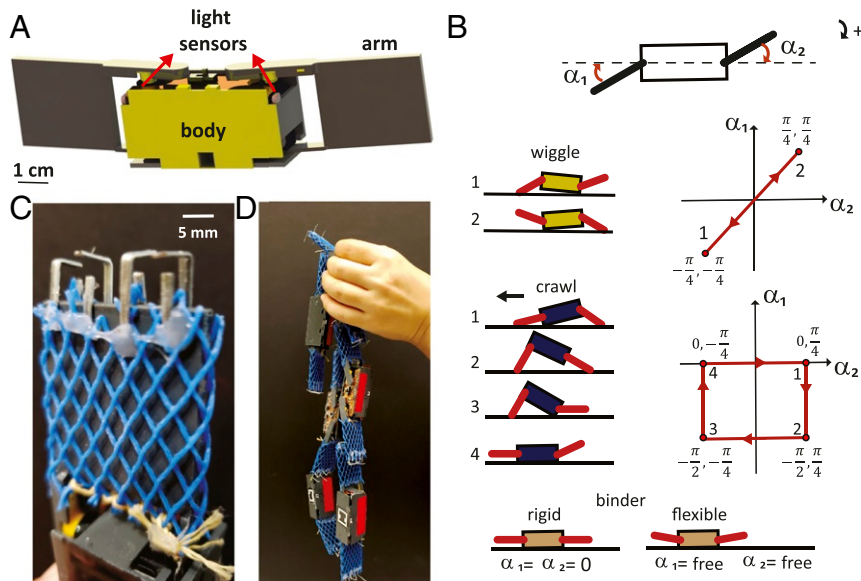


Fig. 5. Robophysical model of a worm blob consisting of three-dimensional (3D) printed robots. (A) Each robot is a three-link, planar robot equipped with two photoresistors and the arms are connected to the body via servos controlled by Arduino Pro-Mini (38). (B) Motion sequences of two gaits as a function of arm angles (α_1 and α_2), wiggle (Top), and crawl (Bottom). We define $\alpha_1 > 0$ when it is above the centerline and $\alpha_2 > 0$ when it is below the center line. The arrows show the direction of the arm movement sequence. Note that the wiggle gait does not lead to forward motion while the crawl does (to the left). For the binder robots, when they are rigid, the robots are powered and their arms are held at the centerline such that $\alpha_{1,2} = 0$, while for the flexible case, the robots are not powered and the arms are free to deform based on interactions with neighboring robots. (C) To enhance the physical entanglement of the robots, the arms are covered with a plastic mesh and L-shape pins are inserted to the edge of the arms. (D) Six robots entangle to form a robophysical model of the worm blob.

the light source (positive phototaxis) (Fig. 5D). By altering the gaits of the robots in response to light (phototaxis) similar to the biological system (worms) that have varying activity levels at different temperatures (thermotaxis), our goal is to establish a robophysical system that allows us to systematically test our mechanistic hypothesis for emergent locomotion in entangled collectives.

Collective Dynamics in Robophysical Blobs. We first demonstrate that strong physical entanglement among individuals is critical for collective locomotion. In previous work (38), robots achieved collective mobility only when they were forced to weakly entangle by an external ring structure. Here, we test the same robots—without any external ring—and since there is little traction (or entanglement) among individuals, it is not possible to create a cohesive robotic blob. Thus, when the robots undergo phototaxis through purely crawl or wiggle gaits, no collective locomotion is observed (SI Appendix, Fig. S14 and Movie S5). To achieve strong entanglements while allowing for ready disentanglement—reflecting the capabilities of the worm blobs—we add a mesh and L-shape pins on the robot arms (Fig. 5C). The size (width = 0.5 cm, length = 1 cm), shape, and orientation of the pins are chosen so that the arms easily attach to and detach from the mesh and form an entangled robotic blob mimicking the worm blobs (see Fig. 5D). For the rest of the robophysical experiments, we use these self-entangling and disentangling robots.

Next, we investigate the collective phototaxis behavior of the robophysical blobs in a quasi-2D confined arena (length = 60 cm, width = 5 cm). We cover the bottom surface of the arena with a mesh to increase substrate friction and place a light source at one end (SI Appendix, Fig. S15A). We expect that the leading robot (closer to the light source, high light intensity) would receive the most light and achieve a crawl gait, while the rearward robots (farther away from light, low light intensity) would execute a wiggle gait. The middle robots that receive intermediate

light intensity would keep their arms rigid, to create a cohesively moving robotic blob. Surprisingly however, we observe that the robotic blob slowly disentangles and the robots move individually toward the light, rather than moving as a group (Fig. 6A). By tracking the arm positions of each robot in a blob using an automated tracking software (DeepLabCut) (57), we observe that although the crawler robots and wiggler robots behave as expected, the intermediate light robots through their rigidity diminish effective force transmission within the blob, leading to disentanglement (SI Appendix, Fig. S16). Once the blob has disentangled, these intermediate robots also change to a crawling gait (no longer shaded from light in the blob) and move individually toward the light source (Movie S5).

To address this issue of disentanglement, we simply switch off a subset of the intermediate light intensity robots to allow them to freely deform their arms (flexible) in response to neighboring robot arm movements (Fig. 6B). Now, the inactive robots (not powered) act as passive and compliant “binders,” enabling the blob to move as a collective, similar to their biological counterparts (Fig. 6C, Right; SI Appendix, Fig. S15; Movie S5; and Table 1). We note that the remaining robots are active (powered) and change their gaits according to the light intensity as described previously (if >900 crawl, <900 wiggle).

Further analysis of the robophysical blob dynamics reveals little change in connectivity (defined as the total number of robots that individual robots touch) between the robots in the “flexible” case ($8.7 \pm 9.0\%$), while in the “rigid” case the robots go from highly connected to spread out ($20.1 \pm 25.1\%$) as shown in SI Appendix, Fig. S18. We also note that the mean displacement of the entire group is quite similar in both cases (flexible, 10.5 ± 4.9 mm; rigid, 9.5 ± 6.0 mm; Fig. 6D); however, the mean displacement differs significantly for individual robots in the rigid case as only one to two robots successfully make it all of the way to the light source as a unit (Fig. 6F). By tracking all robots, we also plot a summary of the distribution of the vertical arm positions with time (Δy) over time (Fig. 6E). When all or most of

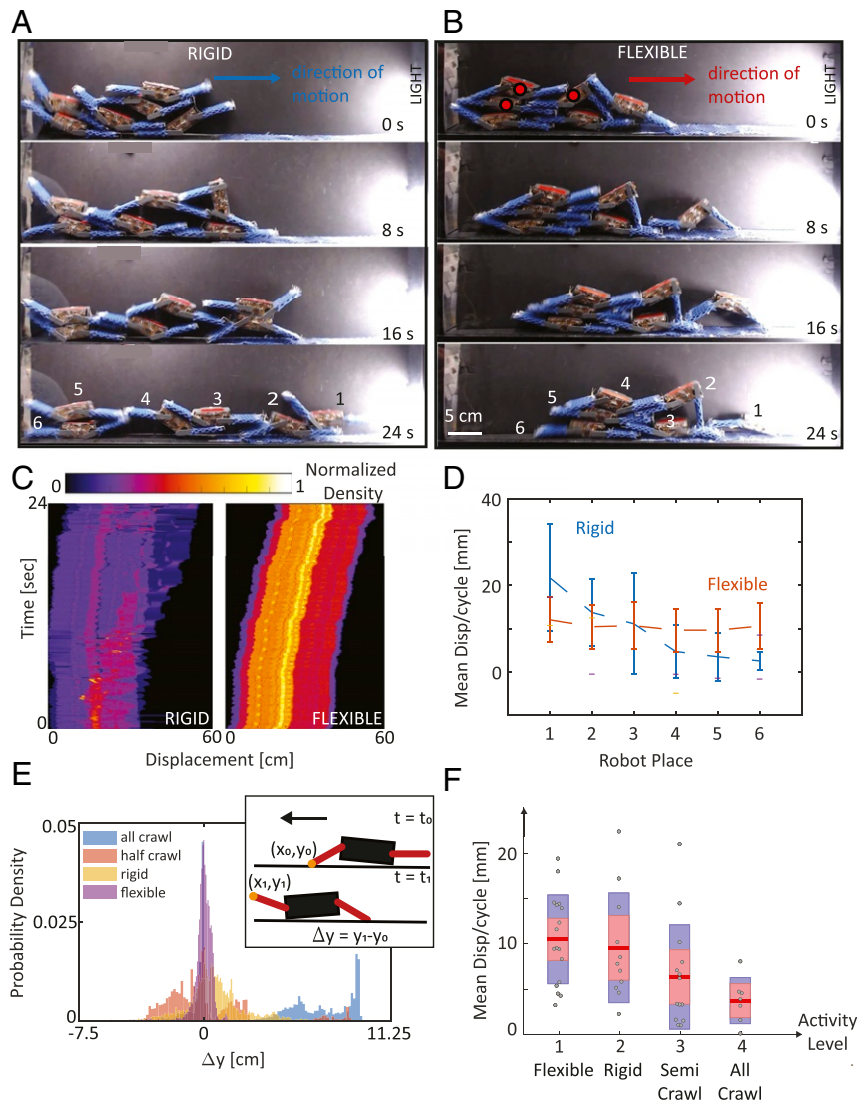


Fig. 6. Collective locomotion of a physically entangled robotic blob. (A) Snapshots from the experiment where all of the robots are active and change their gaits from wiggling (<200 lux) to crawling (>800 lux) according to light intensity (Fig. 5B). At intermediate light intensity (200 to 800 lux) the robots kept their arms straight (rigid), i.e., $\alpha_1 = \alpha_2 = 0$ (Movie S5). (B) The robots with red dots are inactive (unpowered) and their arms can move flexibly to enable them to act as binders for the robotic blob. The remaining robots changed their gaits according to light intensity thresholds described previously (Fig. 5B and Movie S5). (C) Space-time overlap heatmaps of robot positions (x axis), revealing collective motion in the flexible case. Color represents the normalized density of the robots. (D) Mean displacement of the individual robots in a run for the flexible ($n = 17$ trials) and rigid ($n = 11$) cases. (E) Distribution of the vertical arm position $\Delta y = y(t) - y(0)$ with respect to initial arm position of the robots in a blob for four different gaits (blue, all crawl; orange, half crawl; yellow, rigid; purple, flexible). Each dataset has 10,000 data points randomly chosen from two to five experiments. Inset shows schematic illustration of Δy measurement. (F) Mean displacement of all of the robots per cycle in a run for the all crawl ($n = 6$ trials), semicrawl ($n = 15$ trials), flexible ($n = 17$ trials), and rigid ($n = 11$) cases (see Table 1 for the details). The activity level is defined as how much the robots move their arms on a vertical plane.

the robots crawl, the distribution is flattened, resulting in spreading out or disentangling behavior. In the flexible case, we see a narrow distribution, revealing that only a few robots crawl, thus leading to collective transport (Fig. 6E).

We additionally conduct experiments to further reinforce that heterogeneous gait differentiation is critical for collective movement. Since only the crawl gait leads to forward movement (the wiggle gait does not break symmetry), we program all robots to execute only a crawl gait. A purely homogeneous crawl gait leads to disentanglement, where the robots move individually rather than collectively, and only a few robots ultimately reach the end of the arena (3.73 ± 2.5 mm; SI Appendix, Fig. S17A; Movie S5; and Fig. 6E). To create a partial gait heterogeneity, we switch off the robots in the rear (three of six inactive), while the front robots

execute only a crawl gait. We observe a modest improvement, as the robotic collective does move together now (mean displacement per cycle 6.3 ± 5.7 mm; Fig. 6F). A summary of these results is presented in Table 1. Taken together, these results support that a strong physical entanglement and heterogeneous gait differentiation are necessary for collective mobility in the robotic blob.

Finally, to test whether gait differentiation leads to energetic benefits, we measured the power usage of a single robot while performing wiggle and crawl gaits with no additional load on the arms or body. We find that the wiggle gait (240 ± 50 mW) utilizes approximately half the power of the crawl gait (480 ± 150 mW; SI Appendix, Fig. S15D). Although our single-robot measurements suggest that gait differentiation could lead to overall lower

Table 1. Summary of robophysical experiments

Case	Active robots	Gaits of active robots	Dynamic	Figure
Rigid	6	Wiggle crawl, active binder	Disentanglement, individual locomotion	Fig. 6A
Flexible	3	Wiggle crawl, passive binder	Collective locomotion	Fig. 6B and SI Appendix, Fig. S14C
All crawl	6	Crawl	Disentanglement, individual locomotion	SI Appendix, Figs. S14B and S17A
Half crawl	3	Crawl	Inefficient collective locomotion	SI Appendix, Fig. S17B

collective energy consumption, further work needs to be done to measure the in situ power consumption of individual robots under different conditions. We anticipate that by harnessing gait differentiation, future entangled robotic swarms could improve their energy efficiency in addition to exhibiting adaptive and decentralized swarming locomotion.

Concluding Remarks

We performed a functional study on a biological system consisting of a multitude of worms, i.e., a worm blob, to investigate the fundamental mechanisms behind the emergent physical adaptability, mechanofunctionality, and locomotion of the entangled collective. We studied systematically how the worm blob reacts to different environmental stresses depending on the type, history, and intensity of the associated perturbations. We found that a worm blob that moves through the use of physical entanglement and differentiation can protect against desiccation collectively by reducing the size of a blob, which allows emergent behavior even in the absence of centralized control. To validate our hypotheses on the collective locomotion of the worm blob, we used a robophysical model of a blob consisting of six small, three-link robots that can entangle to each other with the help of mesh-covered pinned arms. Our model enabled us to investigate other parameters such as the gaits, activity, and flexibility of the individuals that are challenging to directly test in the living system.

For robotics, the creation of a coherent swarm of simple robots has long been a goal, and our robophysical blob is part of an emerging trend in leveraging mechanics and physics to perform collective tasks in a decentralized way (37, 38) rather than the traditional algorithm-based and centrally controlled approach to swarms (31, 58–64). Typically in robotics, the complex physical interactions between individual robots are either simplified or ignored in idealized theoretical models. Through our robotic blobs, we show the rich behavior that exists between stochastic local interactions between individuals that leads to emergent functionalities of pulling, reducing substrate friction, and even force transmission in a dynamically cohesive robotic blob. These principles can be harnessed in the design of emergent swarm robots for real-world applications.

For biology, the worm blobs hold exciting potential to inspire adaptive active materials as well as advance our understanding of emergent biomechanics of living collectives (16–20). We note that, to the best of our knowledge, the only other entan-

gled assemblage capable of emergent motility occurs at cellular scales, where the amoeboid cells of the slime mold *Dictyostelium discoideum* form a motile slug synchronized by cAMP waves (65). At larger length scales, almost exclusively all known examples of functional self-assembled structures (bivouacs, rafts, bridges, etc.) are observed in insect societies (Phylum: Arthropoda), which, although they can adapt and reconfigure, do not exhibit emergent locomotion of the whole entangled collective (13). Thus, this report contributes a discovery of a physically entangled and self-motile self-assemblage in a non-Arthropod multicellular organism.

While beyond the scope of this paper, we have also observed an impressive array of behaviors in the worm blob system. For example, under uniform temperatures (no gradients) worm blobs extend protrusions from the periphery to execute locomotion in air, which is qualitatively reminiscent of cellular motility, albeit at larger length scales ([SI Appendix, Fig. S3](#)) (66–69). Other behaviors we have observed include food foraging by the blob using the individual worms as appendages as well as locomotion in unstructured three-dimensional environments. Thus, our work paves the way for further discoveries of emergent mechanofunctional behaviors in a seemingly mundane blob of squishy worms.

Materials and Methods

Animal Experiments. *L. variegatus* was obtained from Aquatic Foods & Blackworm Co. The worms (length = 2.5 ± 1 cm, radius = 0.6 ± 0.1 mm, mass = 7.5 ± 3 mg) were cultivated in a box ($35 \times 20 \times 12$ cm, 25 g worms per box) filled with distilled water ($h = \sim 2$ cm) at $\sim 15^\circ\text{C}$ for at least 3 wk prior to experiments. We feed the worms with tropical fish flakes once a week and change the water 1 d after feeding them. Studies with *L. variegatus* do not require approval by the institutional animal care committee.

Analysis of the Data. All of the animal data were analyzed using the MATLAB Image Processing Toolbox. We used DeepLabCut (DLC) software (57) to track the robots' arm positions given in Fig. 6 C and D and [SI Appendix, Fig. S16](#).

Data Availability. All study data are included in this article and/or [SI Appendix](#).

ACKNOWLEDGMENTS. We thank Eva Erickson for helping analyze the robot videos with DLC and Will Savoie, Ross Warkentin, Max Seidel, and Meredith Caveney for early design of smarticles. This work was supported by the Soft Matter Incubator Seed Grant Program of Georgia Institute of Technology. M.S.B. acknowledges funding support from NSF Grants CAREER 1941933 and 1817334.

- J. K. Parrish, L. Edelstein-Keshet, Complexity, pattern, and evolutionary trade-offs in animal aggregation. *Science* **284**, 99–101 (1999).
- M. C. Marchetti *et al.*, Hydrodynamics of soft active matter. *Rev. Mod. Phys.* **85**, 1143–1189 (2013).
- C. Bechinger, R. D. Leonardo, C. Reichardt, G. Volpe, G. Volpe, Active particles in complex and crowded environments. *Rev. Mod. Phys.* **88**, 045006 (2016).
- S. Ramaswamy, The mechanics and statistics of active matter. *Annu. Rev. Condensed Matter Phys.* **1**, 323–345 (2010).
- T. Vicsek, A. Zafeiris, Collective motion. *Phys. Rep.* **517**, 71–140 (2012).
- J. Elgeti, R. G. Winkler, G. Gompper, Physics of microswimmers—single particle motion and collective behavior: A review. *Rep. Prog. Phys.* **78**, 056601 (2015).
- M. Tennenbaum, Z. Liu, D. Hu, A. Fernandez-Nieves, Mechanics of fire ant aggregations. *Nat. Mater.* **15**, 54–59 (2016).
- M. Bross *et al.*, Hydromechanics of fish schooling. *Annu. Rev. Physiol.* **26**, 357 (1967).
- M. Ballerini *et al.*, Interaction ruling animal collective behavior depends on topological rather than metric distance: Evidence from a field study. *Proc. Natl. Acad. Sci. U.S.A.* **105**, 1232–1237 (2008).
- A. Cavagna *et al.*, Scale-free correlations in starling flocks. *Proc. Natl. Acad. Sci. U.S.A.* **107**, 11865–11870 (2010).
- J. K. Parrish, S. V. Viscido, D. Grünbaum, Self-organized fish schools: An examination of emergent properties. *Biol. Bull.* **202**, 296–305 (2002).
- A. Doostmohammadi, J. Ignés-Mullol, J. M. Yeomans, F. Sagués, Active nematics. *Nat. Commun.* **9**, 3246 (2018).
- C. Anderson, G. Theraulaz, J. L. Deneubourg, Self-assemblages in insect societies. *Insectes Soc.* **49**, 99–110 (2002).
- F. J. Vernerey *et al.*, Biological active matter aggregates: Inspiration for smart colloidal materials. *Adv. Colloid Interface Sci.* **263**, 38–51 (2019).
- D. L. Hu, S. Phonekeo, E. Altshuler, F. Brochard-Wyart, Entangled active matter: From cells to ants. *Eur. Phys. J. Spec. Top.* **225**, 629–649 (2016).

16. N. J. Mlot, C. Tovey, D. L. Hu, Dynamics and shape of large fire ant rafts. *Commun. Integr. Biol.* **5**, 590–597 (2012).
17. N. J. Mlot, C. A. Tovey, D. L. Hu, Fire ants self-assemble into waterproof rafts to survive floods. *Proc. Natl. Acad. Sci. U.S.A.* **108**, 7669–7673 (2011).
18. T. Sakiyama, Ant droplet dynamics evolve via individual decision-making. *Sci. Rep.* **7**, 14877 (2017).
19. O. Peleg, J. M. Peters, M. K. Salcedo, L. Mahadevan, Collective mechanical adaptation of honeybee swarms. *Nat. Phys.* **14**, 1193–1198 (2018).
20. F. J. Vernerey, T. Shen, S. L. Sridhar, R. J. Wagner, How do fire ants control the rheology of their aggregations? A statistical mechanics approach. *J. R. Soc. Interface* **15**, 20180642 (2018).
21. R. Di Leonardo, Controlled collective motions. *Nat. Mater.* **15**, 1057–1058 (2016).
22. W. Wang, W. Duan, S. Ahmed, A. Sen, T. E. Mallouk, From one to many: Dynamic assembly and collective behavior of self-propelled colloidal motors. *Accounts Chem. Res.* **48**, 1938–1946 (2015).
23. F. Ginot, I. Theurkauff, F. Detcheverry, C. Ybert, C. Cottin-Bizonne, Aggregation-fragmentation and individual dynamics of active clusters. *Nat. Commun.* **9**, 696 (2018).
24. J. Yu, B. Wang, X. Du, Q. Wang, L. Zhang, Ultra-extensible ribbon-like magnetic microswarm. *Nat. Commun.* **9**, 3260 (2018).
25. Q. Chen, S. C. Bae, S. Granick, Directed self-assembly of a colloidal kagome lattice. *Nature* **469**, 381–384 (2011).
26. M. Brambilla, E. Ferrante, M. Birattari, M. Dorigo, Swarm robotics: A review from the swarm engineering perspective. *Swarm Intell.* **7**, 1–41 (2013).
27. B. Varghese, G. McKee, A mathematical model, implementation and study of a swarm system. *Robot. Auton. Syst.* **58**, 287–294 (2010).
28. M. N. Ab Wahab, S. Nefti-Meziani, A. Atyabi, A comprehensive review of swarm optimization algorithms. *PLoS One* **10**, e0122827 (2015).
29. A. Martinoli, K. Easton, W. Agassounon, Modeling swarm robotic systems: A case study in collaborative distributed manipulation. *Int. J. Robot. Res.* **23**, 415–436 (2004).
30. A. Prorok, N. Correll, A. Martinoli, Multi-level spatial modeling for stochastic distributed robotic systems. *Int. J. Robot. Res.* **30**, 574–589 (2011).
31. M. Rubenstein, A. Cornejo, R. Nagpal, Programmable self-assembly in a thousand-robot swarm. *Science* **345**, 795–799 (2014).
32. A. Kushleyev, D. Mellinger, V. Kumar, Toward a swarm of agile micro quadrotors. *Aut. Robots* **35**, 287–300 (2013).
33. T. Sawetzki, S. Rahmouni, C. Bechinger, D. W. Marr, In situ assembly of linked geometrically coupled microdevices. *Proc. Natl. Acad. Sci. U.S.A.* **105**, 20141–20145 (2008).
34. M. A. Hsieh, V. Kumar, L. Chaimowicz, Decentralized controllers for shape generation with robotic swarms. *Robotica* **26**, 691–701 (2008).
35. D. Saldana et al., “A decentralized algorithm for assembling structures with modular robots” in *Proceedings of the 2017 IEEE International Conference on Intelligent Robots and Systems*, (Institute of Electrical and Electronics Engineers Inc., Piscataway, NJ, 2017), vol. 2017, pp. 2736–2743.
36. B. Gabrich, D. Saldana, V. Kumar, M. Yim, “A flying gripper based on cuboid modular robots” in *Proceedings of the 2018 IEEE International Conference on Robotics and Automation* (ICRA, Piscataway, NJ, 2018), pp. 7024–7030.
37. S. Li et al., Particle robotics based on statistical mechanics of loosely coupled components. *Nature* **567**, 361–365 (2019).
38. W. Savoie et al., A robot made of robots: Emergent transport and control of a smarticle ensemble. *Sci. Robot* **4**, 4316 (2019).
39. J. Aguilar et al., A review on locomotion robotics: The study of movement at the intersection of robotics, soft matter and dynamical systems. *Rep. Prog. Phys.* **79**, 110001 (2016).
40. Y. Ozkan-Aydin, J. M. Rieser, C. M. Hubicki, W. Savoie, D. I. Goldman, “Physics approaches to natural locomotion: Every robot is an experiment” in *Robotic Systems and Autonomous Platforms*, S. M. Walsh, M. S. Strano, Eds. (Elsevier, 2019), pp. 109–127.
41. A. Deblais, S. Woutersen, D. Bonn, Rheology of entangled active polymer-like *T. tubifex* worms. *Phys. Rev. Lett.* **124**, 188002 (2020).
42. C. D. Drewes, C. R. Fournier, Hindsight and rapid escape in a freshwater oligochaete. *Biol. Bull.* **177**, 363–371 (1989).
43. T. Timm, P. J. Martin, “Clitellata: Oligochaeta” in *Thorpe and Covich’s Freshwater Invertebrates* (Fourth Edition), J. H. Thorpe, D. C. Rogers, Eds. (Academic Press, 2015), pp. 529–549.
44. R. O. Brinkhurst and B.G.M. Jamieson, *Aquatic Oligochaeta of the World*, D. G. Cook, D. V. Anderson, J. Van der Land, Eds. (Oliver and Boyd, Edinburgh, University of Toronto Press, Toronto, 1971).
45. C. D. Drewes, R. O. Brinkhurst, Giant nerve fibers and rapid escape reflexes in newly hatched aquatic oligochaetes, *Lumbriculus variegatus* (family Lumbriculidae). *Invertebr. Reprod. Dev.* **17**, 91–95 (1990).
46. A. Deblais, A. C. Maggs, D. Bonn, S. Woutersen, Phase separation by entanglement of active polymerlike worms. *Phys. Rev. Lett.* **124**, 208006 (2020).
47. C. Fillafer, M. F. Schneider, On the temperature behavior of pulse propagation and relaxation in worms, nerves and gels. *PLoS One* **8**, e66773 (2013).
48. M. E. Cates, J. Tailleur, Motility-induced phase separation. *Annu. Rev. Condensed Matter Phys.* **6**, 219–244 (2015).
49. E. R. Trueman, *The Locomotion of Soft-Bodied Animals* (A Series of Students Texts in Contemporary Biology, American Elsevier Publishing Company, New York, NY, 1975).
50. J. H. Crowe, K. A. C. Madin, Anhydrobiosis in nematodes: Evaporative water loss and survival. *J. Exp. Zool.* **193**, 323–333 (1975).
51. L. M. Higa, C. Z. Womersley, New insights into the anhydrobiotic phenomenon: The effects of trehalose content and differential rates of evaporative water loss on the survival of *Opaphelenchus avenae*. *J. Exp. Zool.* **267**, 120–129 (1993).
52. T. Sugi, H. Ito, M. Nishimura, K. H. Nagai, *C. elegans* collectively forms dynamical networks. *Nat. Commun.* **10**, 683 (2019).
53. S. S. Ding, L. J. Schumacher, A. E. Javer, R. G. Endres, A. E. Brown, Shared behavioral mechanisms underlie *C. elegans* aggregation and swarming. *eLife* **8**, e43318 (2019).
54. E. Demir, Y. I. Yaman, M. Basaran, A. Kocabas, Dynamics of pattern formation and emergence of swarming in *C. elegans*. *eLife* **9**, e52781 (2020).
55. C. D. Drewes, C. R. Fournier, Hindsight and rapid escape in a freshwater oligochaete. *Biol. Bull.* **177**, 363–371 (1989).
56. C. Drewes, K. Cain, C. Drewes, K. Cain, As the worm turns: Locomotion in a freshwater oligochaete worm. *Am. Biol. Teach.* **61**, 438–442 (2012).
57. A. Mathis et al., DeepLabcut: Markerless pose estimation of user-defined body parts with deep learning. *Nat. Neurosci.* **21**, 1281–1289 (2018).
58. M. R. Hanlin Wang, Shape formation in homogeneous swarms using local task swapping. *IEEE Trans. Robot.* **36**, 597–612 (2020).
59. W. Li, M. Gauci, R. Gross, Turing learning: A metric-free approach to inferring behavior and its application to swarms. *Swarm Intell.* **10**, 211–243 (2016).
60. L. Garattoni, M. Birattari, Autonomous task sequencing in a robot swarm. *Sci. Robot.* **3**, eaat0430 (2018).
61. J. McLurkin, E. D. Demaine, “A distributed boundary detection algorithm for multi-robot systems” in *Proceedings of the 2009 IEEE/RSJ International Conference on Intelligent Robots and Systems (IROS)*, Piscataway, NJ, 2009, pp. 4791–4798.
62. S. Jones, A. F. Winfield, S. Hauert, M. Studley, Onboard evolution of understandable swarm behaviors. *Adv. Int. Syst.* **1**, 1900031 (2019).
63. F. Arvin et al., Mona: An affordable open-source mobile robot for education and research. *J. Int. Robot. Syst.* **94**, 761–775 (2019).
64. M. Santos, Y. Diaz-Mercado, M. Egerstedt, Coverage control for multirobot teams with heterogeneous sensing capabilities. *IEEE Robot. Automation Lett.* **3**, 919–925 (2018).
65. J. T. Bonner, *The Social Amoebae: The Biology of Cellular Slime Molds* (Princeton University Press, 2009).
66. J. Bereiter-Hahn, Mechanics of crawling cells. *Med. Eng. Phys.* **27**, 743–753 (2005).
67. R. Ananthakrishnan, A. Ehrlicher, The forces behind cell movement. *Int. J. Biol. Sci.* **3**, 303–317 (2007).
68. B. Carlson, S. H. Soderling, Mechanisms of cellular protrusions branch out. *Dev. Cell* **17**, 307–309 (2009).
69. A. D. Bershadsky, M. M. Kozlov, Crawling cell locomotion revisited. *Proc. Natl. Acad. Sci. U.S.A.* **108**, 20275–20276 (2011).

1

2 **Supplementary Information for**

3 **Collective dynamics in entangled worm and robot blobs**

4 **Yasemin Ozkan-Aydin, Daniel I. Goldman, M. Saad Bhamla**

5 **Corresponding Author: M. Saad Bhamla**

6 **E-mail: saadb@chbe.gatech.edu**

7 **This PDF file includes:**

8 Figs. S1 to S18 (not allowed for Brief Reports)

9 Legends for Movies S1 to S6

10 SI References

11 **Other supplementary materials for this manuscript include the following:**

12 Movies S1 to S6

13 **1. List of supplementary videos**

- 14 1. **Movie 1: Entanglement, blob formation and material properties of the worm blob** (1) Blob
15 formation in water starting with untangled state (30°C). (2) ~50K worms form a viscoelastic blob. (3)
16 Viscosity, elasticity and reversible state transition of the worm blob.
- 17 2. **Movie 2: Evaporation response of a worm blob.** (1) A single and thousand worms respond the
18 desiccation. (2) Search and shrink behavior of the worm blob (~100 worms) under room light. (3) Shape
19 changes of the worm blob in water and in air under spotlight. (4) Reversible evaporation response of the
20 worm blobs under room light. (5) Entangled aggregation behavior of other annelids (*L. terrestris* and *E.*
21 *fetida*)
- 22 3. **Movie 3: Phototaxis and thermotaxis responses of a worm blob.** (1) Temperature response of a
23 single worm. (2) Contraction of a worm blob under different light history. (3) Collective locomotion under
24 thermal and light stress.
- 25 4. **Movie 4: Locomotion mechanism under thermal stress via differentiation in function of regions**
26 **of a blob and entanglement.** (1) Pull-push mechanism of a worm blob (~ 20 worms) under thermal
27 stress. (2) Locomotion of a worm blob (~300 worms) under thermal stress. (3) Pulling forces of a single
28 worm in cold and hot water.
- 29 5. **Movie 5: Mechanical interactions and collective movement of a physically-entangled robotic**
30 **blob.** (1) Crawl and wiggle gaits. (2) Differentiation mechanism. (3) Moving as a blob or individually
31 depending on the activity of the robots.
- 32 6. **Movie 6: Collective movement range of a physically-entangled worm blob.** The videos of the
33 worm blob motion (Fig.4D) in four extreme cases.

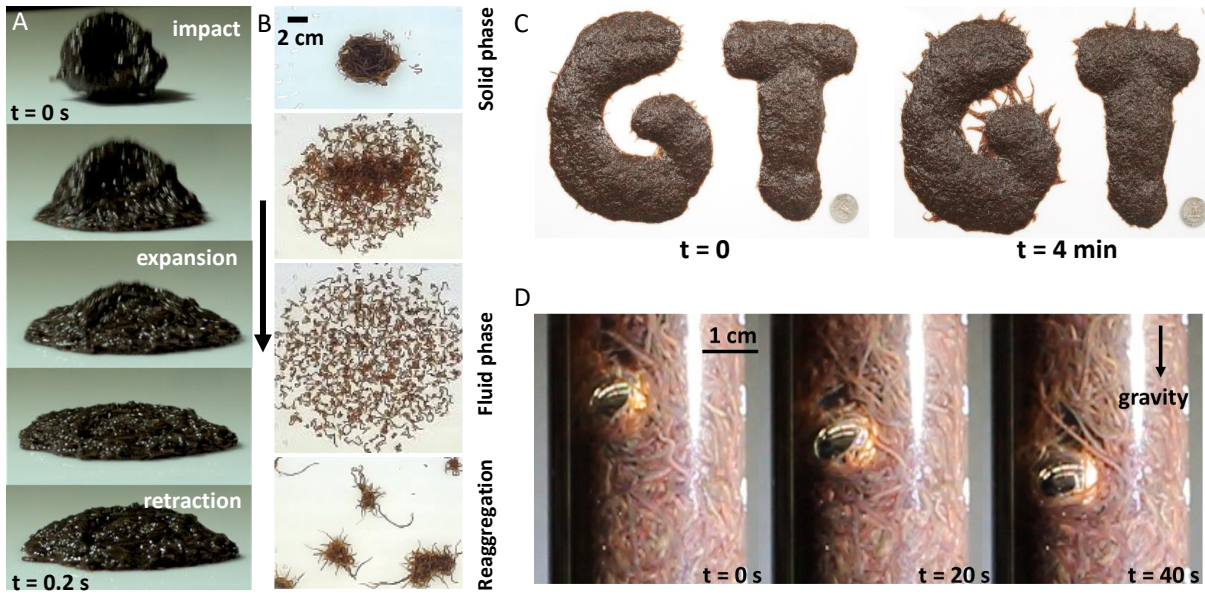


Fig. S1. Material properties of the worm blob– **A.** The worm blob (consists of 5gr. alive worms) was dropped from 30 cm height. When the droplet comes into contact with a hard surface, it expands and retracts in 200 ms. The resulting worm aggregation exhibits elastic behavior. **B.** Solid and fluid-like behavior of worm blob in water. Immediately, after we put the worm blob into the water (temperature is about $\sim 32^\circ\text{C}$), the individual worms in the blob disentangle and changes the state of the blob from solid to fluid. The state transition is reversible. After adding cold water, they started to aggregate and create small blobs in 15 min (bottom). **C.** 3D living sculptures with 50k worms. **D.** The steel sphere of diameter 1.2 cm with a density of $\rho_{\text{sphere}} \approx 7.5 \text{ g cm}^{-3}$ is placed on top of a worm aggregation ($\rho_{\text{worm}} \approx 1 \text{ g cm}^{-3}$) inside a glass measuring tube ($d = 3.5 \text{ cm}$). The gravitational acceleration is $g = 10^3 \text{ cm s}^{-2}$. The sphere falls through the aggregation along vertical direction with a speed about $v \approx 0.025 \text{ cm s}^{-1}$. Using this experiment, we can estimate the bulk viscosity of the worm blob to be $\mu \sim 10,000 \text{ Pa.s.}$ (see SI Appendix, Movie S1). The viscosity μ is estimated as a balance between the net gravitational force and Stokes drag, as done previously for fire ant aggregations, $\mu = (\rho_s - \rho)gr^2/u$ (1).

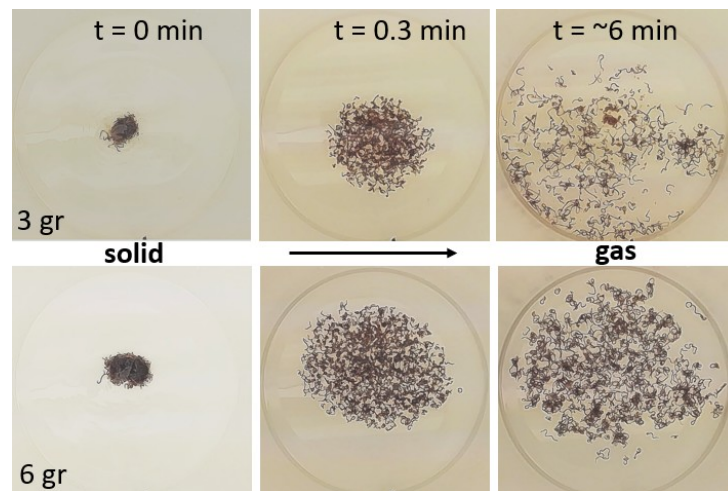


Fig. S2. State transition of a worm blob– A. Solid-to-liquid-to-gas transition of worm blobs with 3 gr (top) and 6 gr (bottom) worms in hot water ($\sim 32^{\circ}\text{C}$). Blob disperses starting from the edges and the diameter of a circle that encloses all the worms grows until its equilibrium size which depends on the initial number of the worms in a blob. After waiting for a long time (~ 6 min), the final size reaches the size of the box they were put.

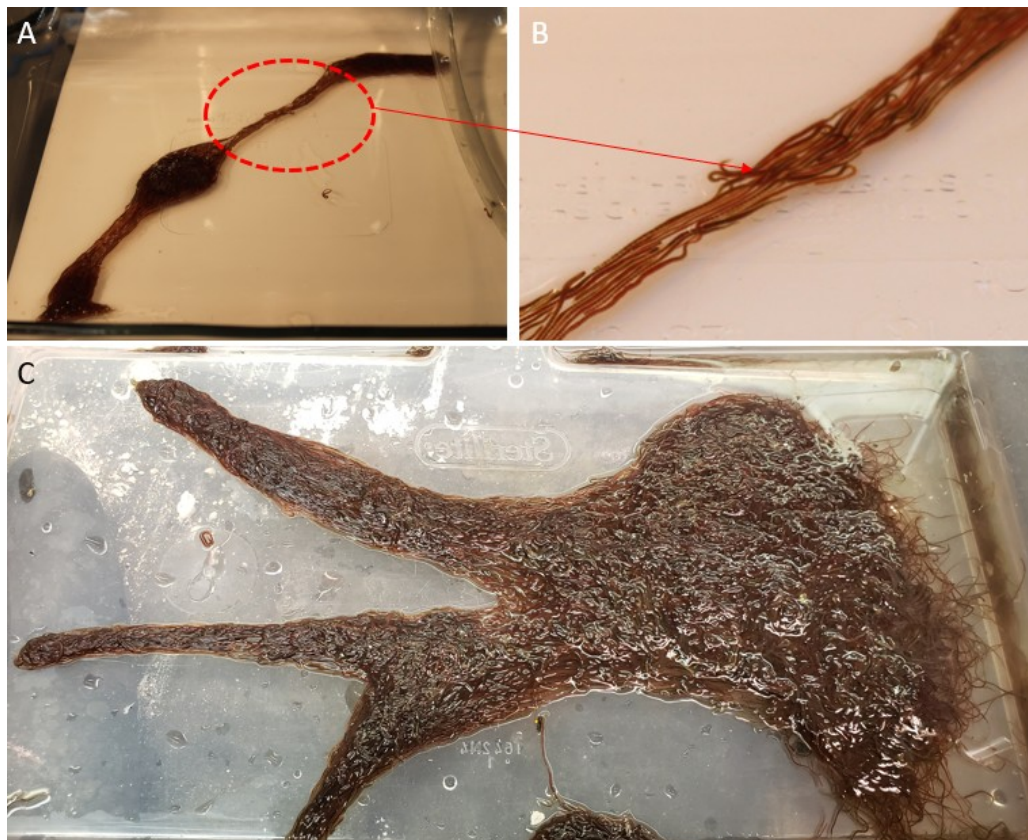


Fig. S3. Locomotion of the worm blob in air– **A.** In air(24°C), the worms form a nematic alignment to migrate from center to corner of the box. **B.** Zoomed image bridge between the center and corner blob shows the alignment. **C.** Thousands of worms break symmetry by extending protrusions on the edge in the direction of the locomotion.

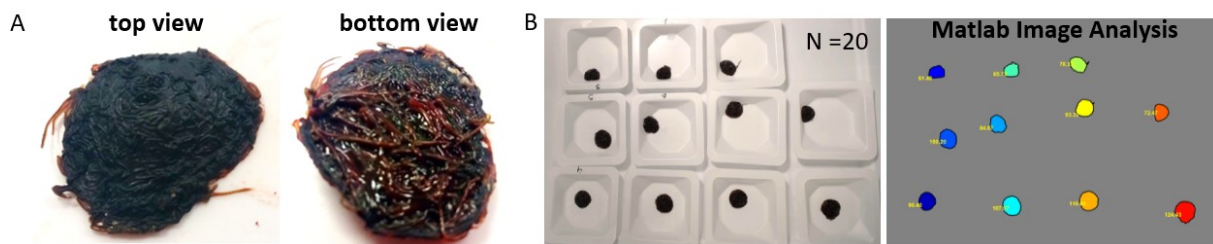


Fig. S4. Shape changes of the worm blob under evaporation stress– **A.** After 18 hours although the top layer of the worm blob with 1000 worms dried, inside the worm blob about $\sim 25\%$ of the worms were still alive. This experiment shows the other protective function of the blob. **B.** Example image analyzing with Matlab Image Processing toolbox. The projected surface area of the worm blobs were calculated using built-in *regionprops* function.

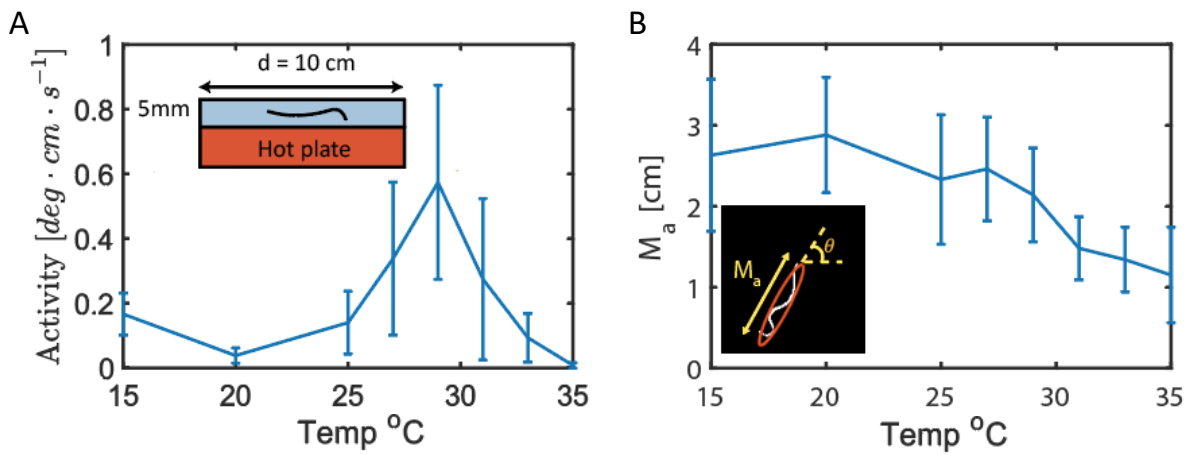


Fig. S5. The temperature response of a single worm– Single worm was placed into petri dish ($d = 10$ cm) filled with water ($h = 5$ mm). The temperature of the hot plate was adjusted and we waited 5 min until the temperature of the water settling at the desired value ($T = 15, 20, 25, 27, 29, 31, 33, 35$). We put a single worm to the water and recorded a 5 min video in each temperature settings. **A.** We calculated the activity which is defined as a multiplication of change of the orientation (θ) and position of a center of mass (CoM) (see inset of SI Appendix, Fig.S5B) as a function of the water temperature. To avoid transient response, we used second half of the recorded videos. The worms are most active at around 30°C . **B.** The major axis of the worms decreases with the temperature. The worms are more elongated in cold (around $\sim 20^\circ\text{C}$) water and started to shrink and curl up as the temperature increases (see SI Appendix, Movie S2).

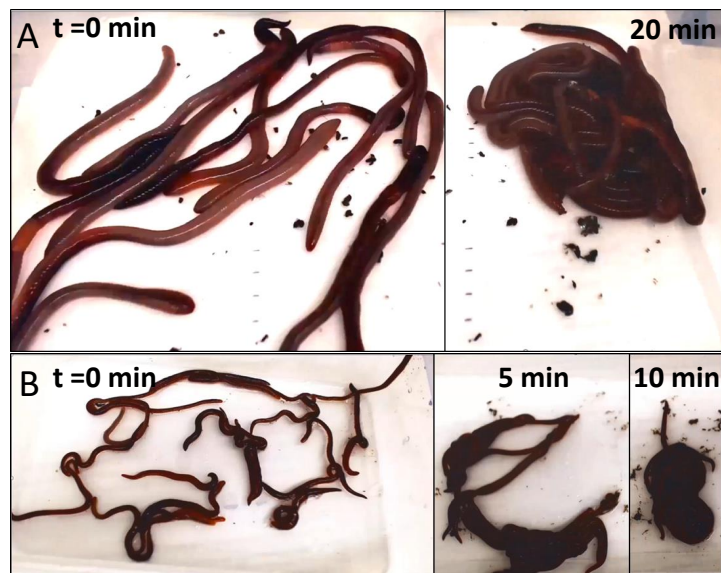


Fig. S6. Blob formation in other type of worms– Blob formation is a stereotype behavior for other type of the worms. **A.** 13 earthworms (*Lumbricus terrestris*) with a length $l = 19 \pm 2$ cm were placed in a dry 20x30 cm box. They formed blob in 20 minutes. **B.** Same experiment was done with 23 red wigglers (*Eisenia fetida*) with a length $l = \pm 2$ cm. After 10 minutes they formed a blob (see SI Appendix, Movie S2).

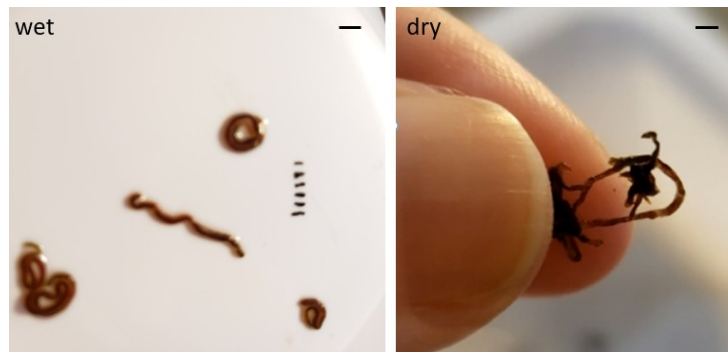


Fig. S7. Individual worm diameter before and after evaporation– The radius of ten worms measured before (left) and after (right) evaporation (about four hours). The radius decreases from $6 \pm 0.1\text{mm}$ to $0.3 \pm 0.1\text{mm}$. The data used in the simulation results given in Fig.2D. Scale bars are equal to 2 mm.

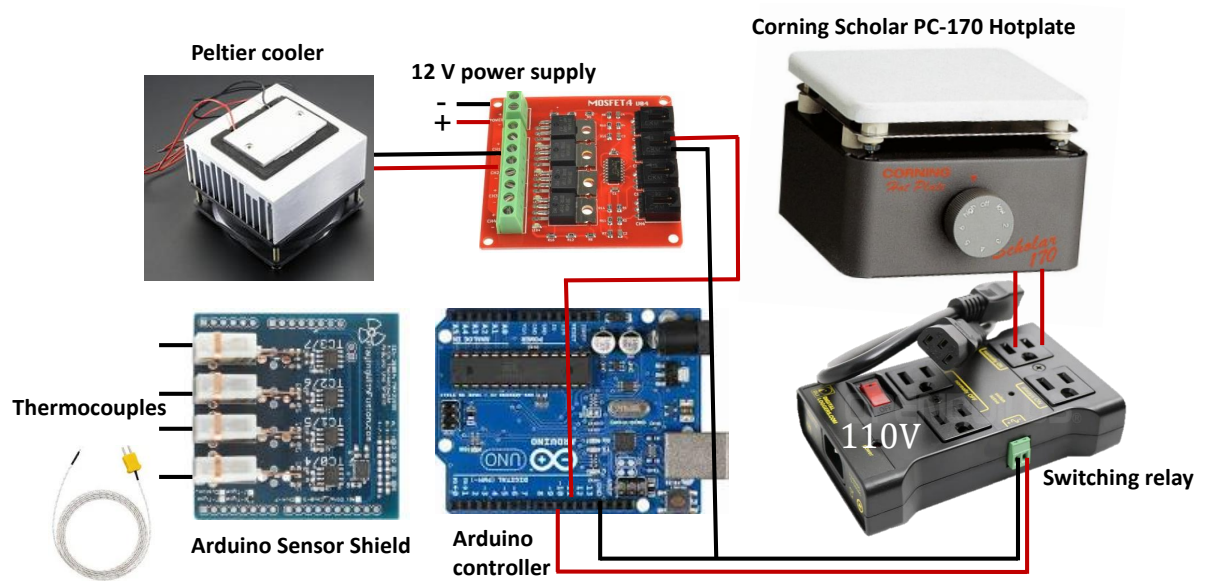


Fig. S8. The details of 3D thermal gradient setup– To measure and control the temperature, two K-type thermocouples (Uxcell) were placed the two edges of the plate. Arduino sensor shield (playwithfusion.com, MAX31855 K-Type Thermocouple Sensor Breakout 4ch) used to collect data from the thermocouples. The peltier cooler (Adafruit) is swithed on/off with four channel MOSFET IRF540 and hot plate is switched on/off with switching relay(Openbuilds, IOT Switching Relay Power Strip), which are controlled by Arduino.

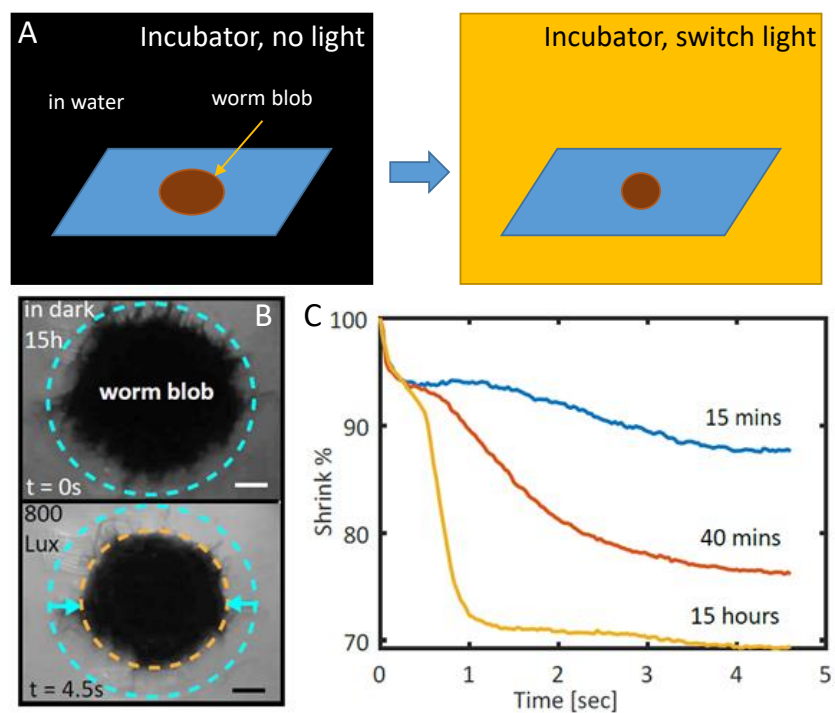


Fig. S9. Light response of the worm blob– **A.** The worm blob was kept in dark in a temperature and humidity controlled incubator for a certain time and then we switched on the light. We measured the projected area of the blob for 5 sec. **B.** Phototaxis behaviour of the worm blob. Time snapshot from the experiment (top view) where worm blob were kept in the dark incubator for 15 hours and the light source (800 Lux) was turned on. The blob shrank about 30% of its initial size. **C.** Phototaxis behaviour of the worm blob under different light stimulus history (duration of the time in the dark, see SI Appendix, Movie S3) .

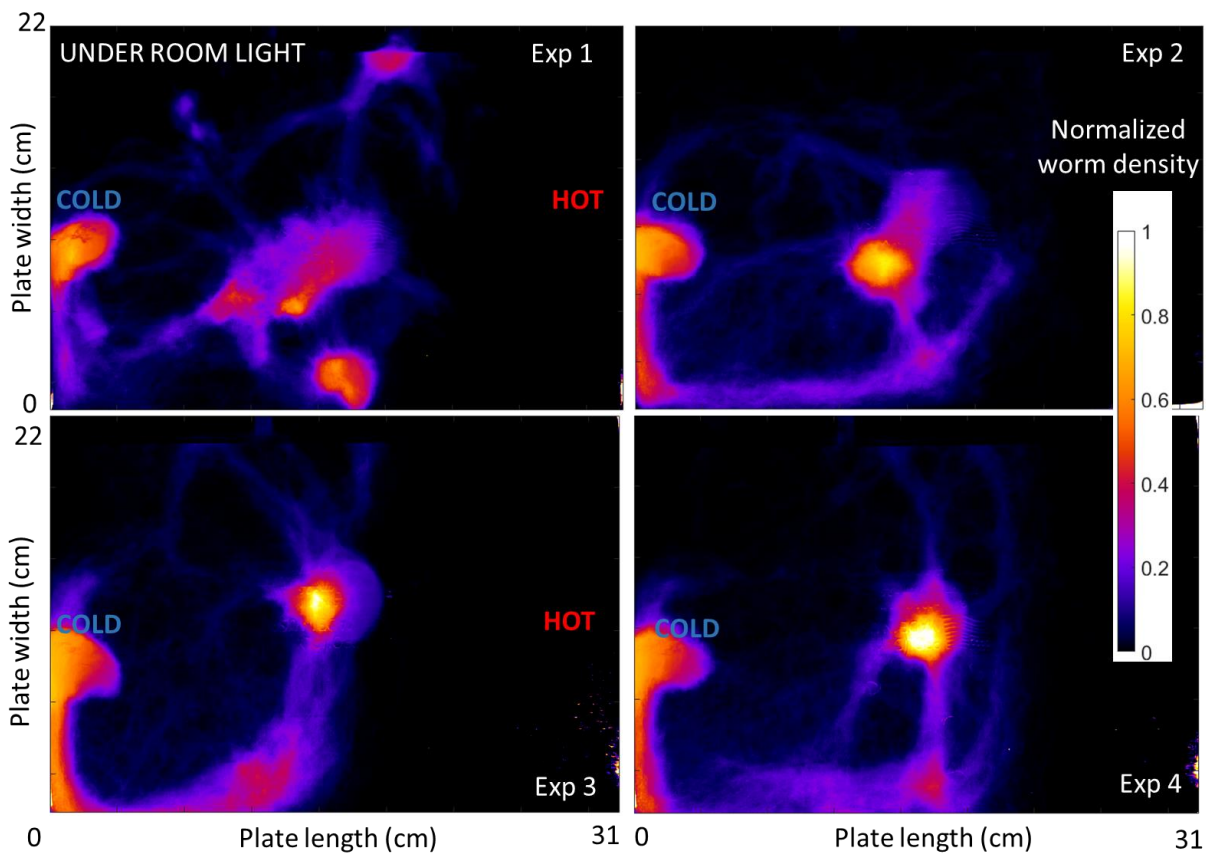


Fig. S10. Experimental space-time overlap heat maps of blob locomotion under ambient light– The thermal gradient setup (left-cold, right-hot) used in this experiments is given in Fig.3A. At each time step, the density of the worms in the plate was calculated by counting black pixels and we plotted normalized pixel numbers at the end. Four panels show the results of four different experiments. The color bar represent normalized worm density (light color represents the most visited area). The heat map shows that the worms are moving individually.

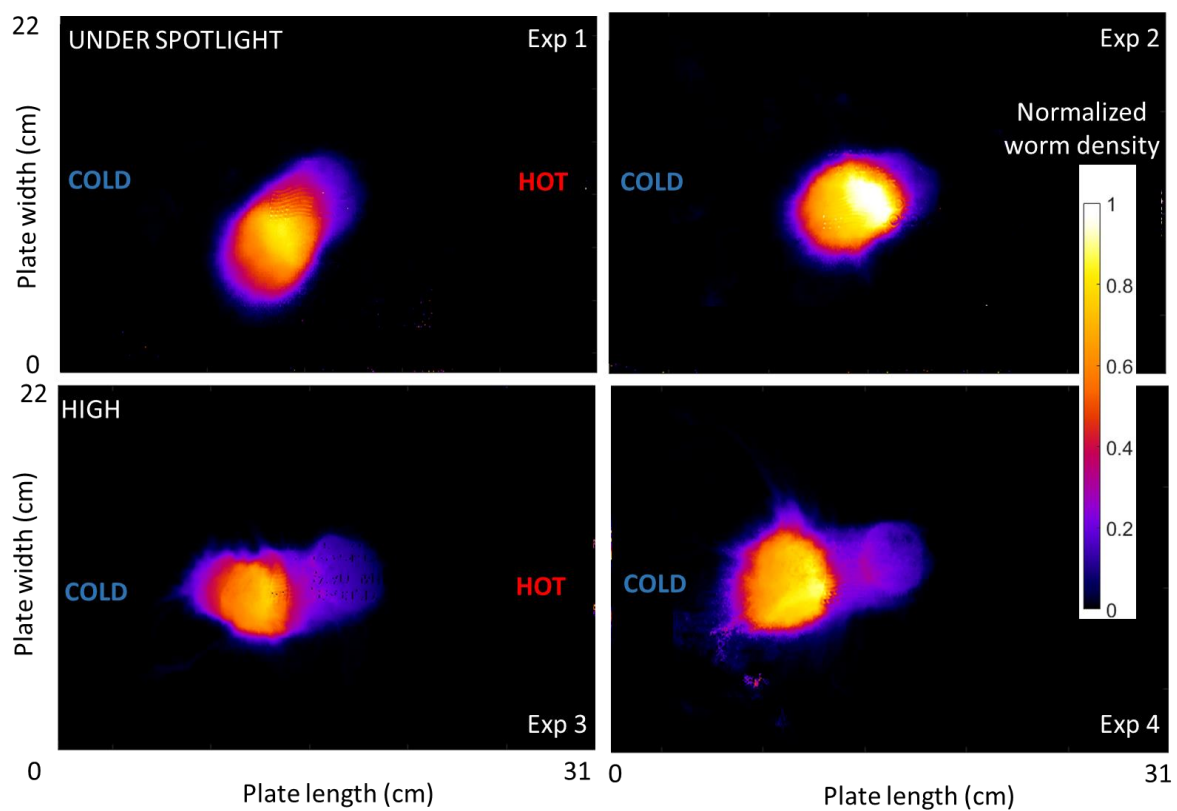


Fig. S11. Experimental space-time overlap heat maps of blob locomotion under spot light– The thermal gradient setup (left-cold, right-hot) used in this experiments is given in Fig.3A. At each time step, the density of the worms in the plate was calculated by counting black pixels and we plotted normalized pixel numbers at the end. Four panels show the results of different experiments under 1500 Lux (top row) and 5500 Lux (bottom row) light intensity. The color bar represent normalized worm density (light color represents the most visited area). The heat map shows that the blob is moving as a group.

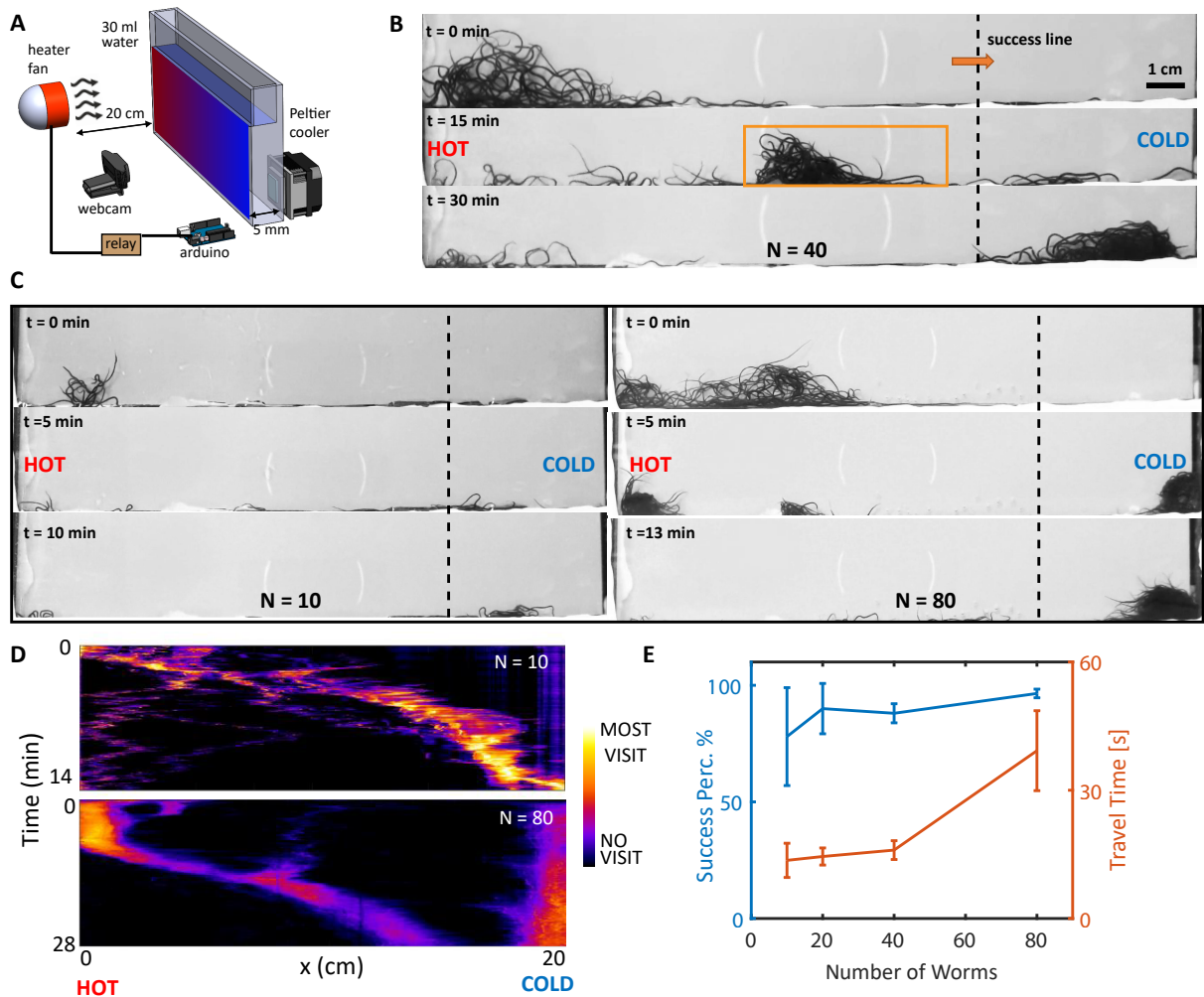


Fig. S12. Quasi 2D thermal response of the worm blob. **A.** Experimental setup for quasi-2D thermal gradient experiments. The heater fan placed 20 cm away from the other side was activated for 10 seconds in every minute with an Arduino controller to create dynamic temperature gradient through the box. **B.** Time snapshot from the quasi-2D experiment (N = 40 worms). Right side of the dashed line shows the safe area used for calculation of the success percentage. **C.** Time snapshot from the quasi-2D experiment (N = 10 (left) and N = 80 (right) worms). **D.** Space-time overlap heat maps of blob locomotion (N = 10 (top) and N = 80 (bottom)). At each time step, the density of the worms in the plate was calculated by counting black pixels and we plotted normalized pixel numbers at the end. The color bar represent normalized worm density (light color represents the most visited area). **E.** Travel time (blue) and success percentage (red - defined as the percentage of the worms that crawl to cold side) vs. number of worms (10, 20, 40 and 80), averaged over 5 experiments per each size.

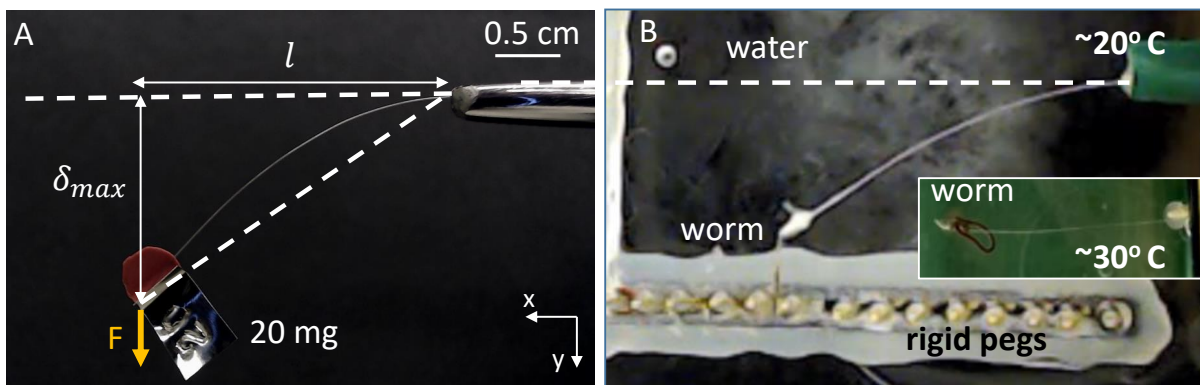


Fig. S13. Single worm pulling force measurement in different temperature—A. We calculated the flexural rigidity (EI) of a stainless steel ($l=3$ cm, $d = 0.1143$ mm, A-M Systems, Inc., WA) beam by applying known perpendicular external loads (F) to the tip of the beam (see SI Appendix, Movie S4). The external force generated by the worm then can be calculated by the deflection formula $F = \frac{\delta_{max} 3EI}{l^3}$, where δ_{max} is the maximum deflection of the tip of the beam B. Snapshot from one of the experiment where the worm apply maximum pulling force in cold water ($\sim 20^\circ$). Inset shows the curled shape of the worm in hot water ($\sim 30^\circ$).

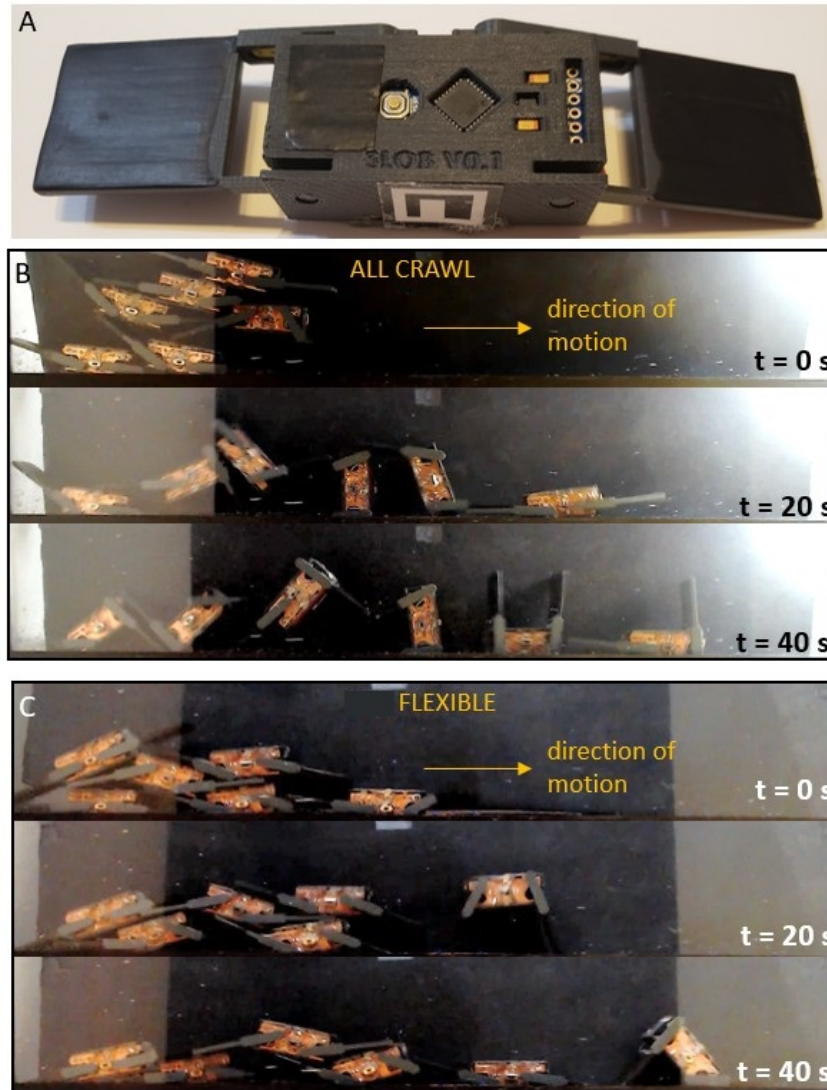


Fig. S14. Control experiments with unentangled armed robots– The robots with plain arms (A) (the arms do not have mesh and pins) tested with two scenarios. **B.** All robots use crawling gait. Mean displacement of all the robots is 6.2 ± 2.9 mm/cycle **C.** Front robot crawls, and bottom two robots wiggle. Others are inactive. Mean displacement of all the robots is 4.1 ± 1.3 mm/cycle. All experimental results are the mean of three runs.

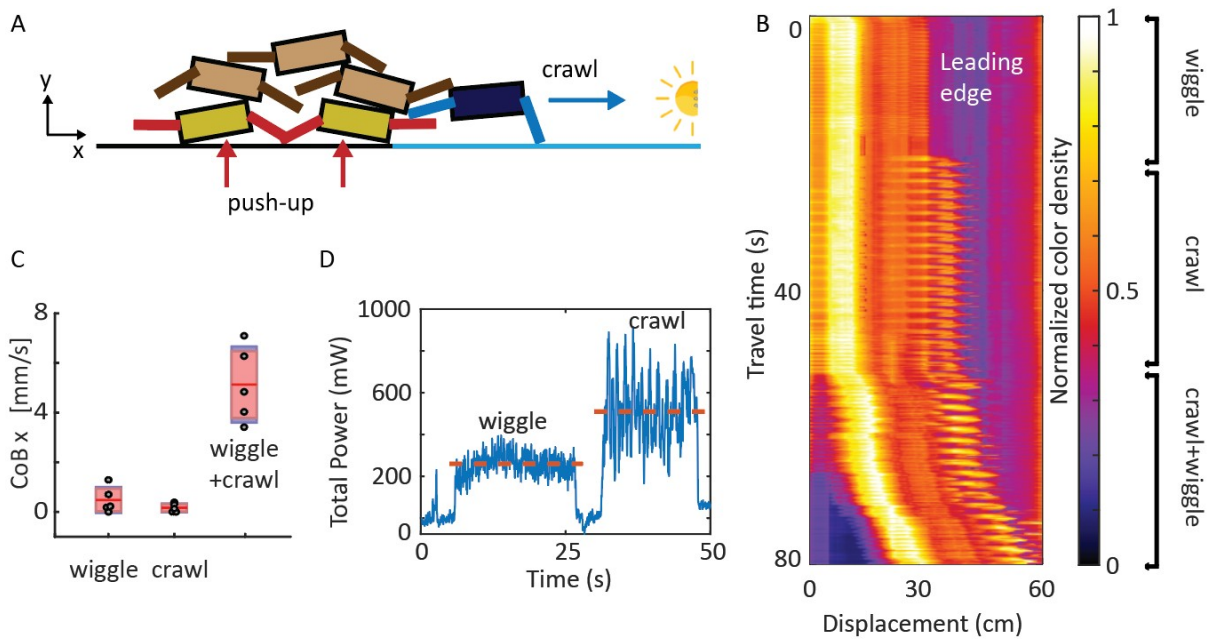


Fig. S15. Mechanical interactions and collective movement of a physically-entangled robotic blob. **A.** Schematic of the robotic test arena, where the first half of the surface (blue) is covered with a mesh to increase substrate friction and a light source is used to activate different gaits (phototaxis). The leading robot (blue) crawls towards to light, bottom robots (yellow) wiggle to push up the center of mass of the blob. Other robots (brown) remain completely or partially immobile during the experiment by keeping arms either rigid or flexible. **B.** Combined space-time plot of the 3-condition experiment shown in SI Appendix, Movie S5, where only the bottom yellow robots wiggle (0-20s), only leading blue robot crawls (20-50s), and both yellow robots wiggle + leading blue robot crawls at the same time (50-80s). We note that only when differentiation of gait occurs in the entangled robotic blob (crawl + wiggle), do we observe directed motion towards the light. Color bar shows the normalized color density of the robots and the setup. **C.** The comparison of the mean and standard deviation of a displacement of the CoB of the robotic blob over 6 test runs for 3 conditions: only bottom yellow robots wiggle, only leading blue robot crawls, and both blue robot crawls + bottom yellow robot wiggle simultaneously (SI Appendix, Movie S5). The red lines represent the mean value, the red area represents the 95% confidence interval, and the blue area represents the mean \pm one standard deviation. **D.** Instantaneous power consumption of the robot during wiggling and crawling gaits. The results are the average of three experiments. Red dashed line shows the mean.

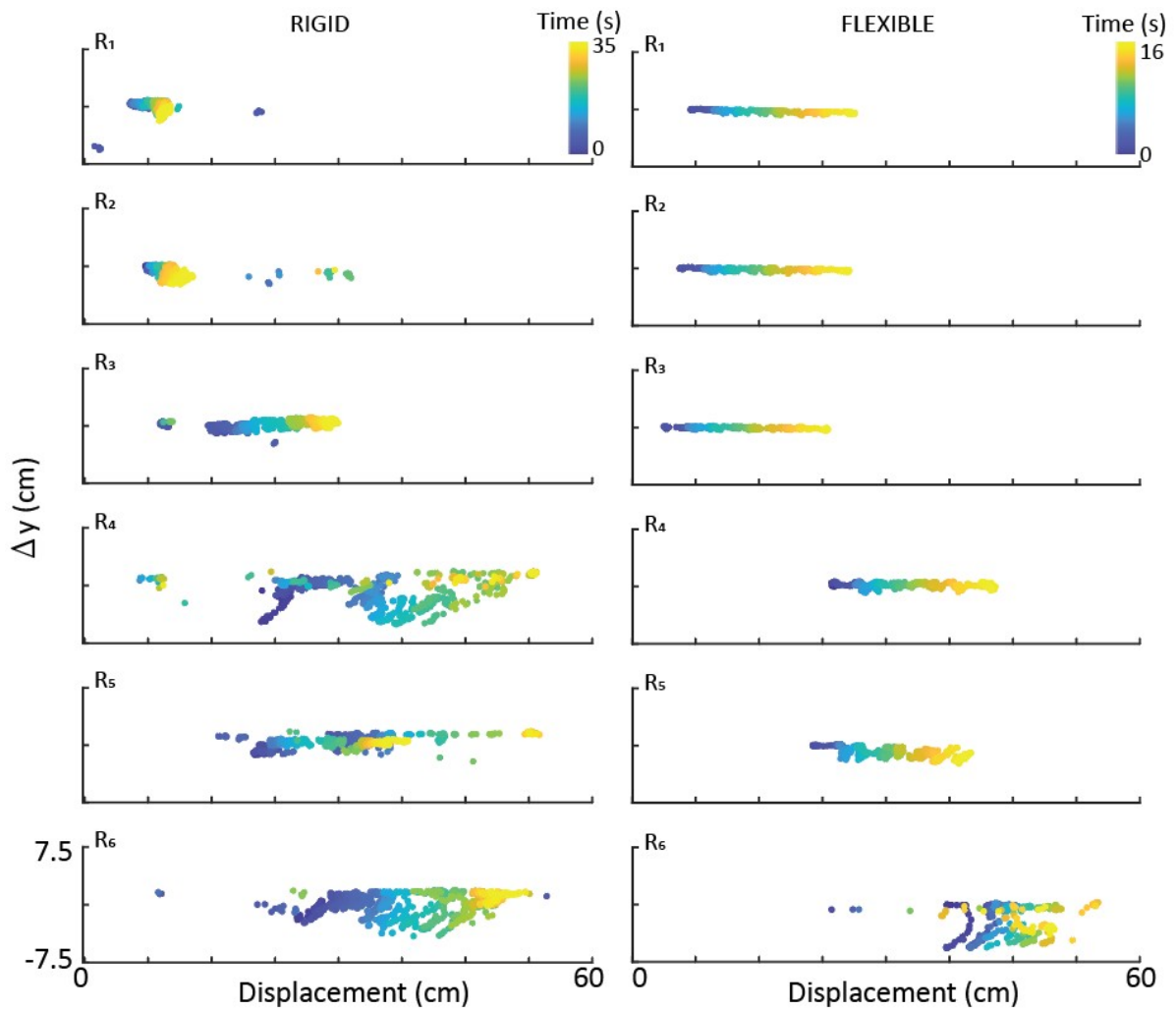


Fig. S16. Relative displacement of the front arm's tip of the robots during time We tracked the tip position of the front arm of each robot (R_1 to R_6) using DeepLabCut (DLC) software. Plots show the relative y distance ($y(t) - y(0)$) vs. forward displacement of the front arm for the rigid (left) and flexible (right) cases during the time (color bar represents the time). The experiments were chosen randomly from the experimental set. All of the axes ranges (x and y) are the same as the bottom left graph.

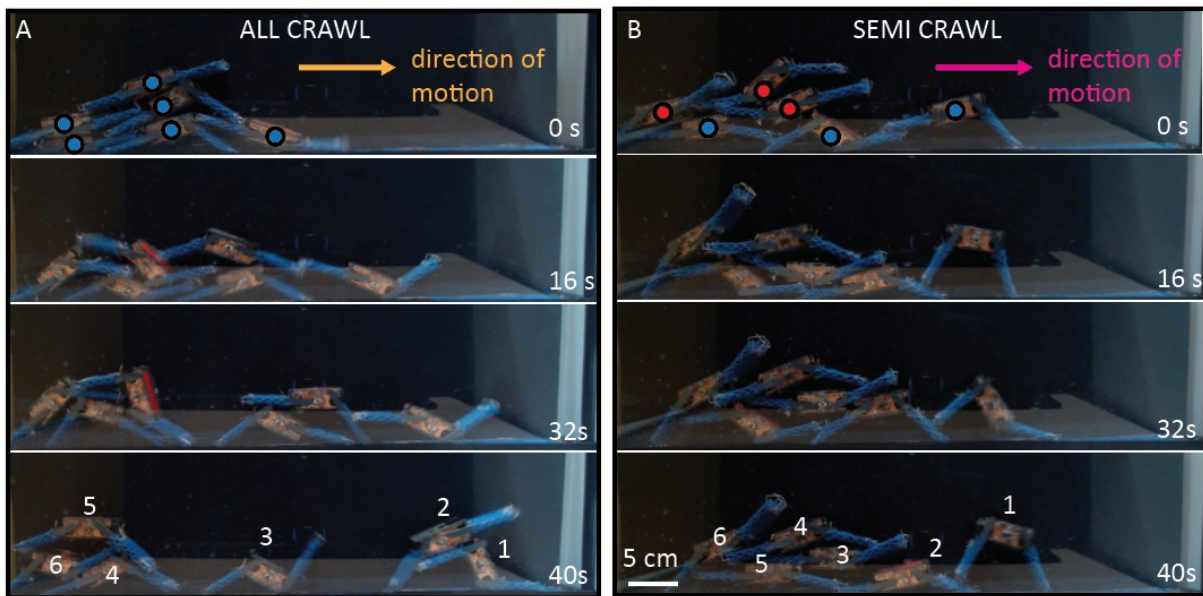


Fig. S17. Gait differentiation of a physically-entangled robotic blob. **A.** Snapshots from the experiment where all the robots (with blue dots) were active and used crawling gait described in Fig. 5D. **B.** Snapshots from the experiment where only the robots with blue dots were active and used crawling gait and others (with red dot) were inactive (see SI Appendix, Movie S5).

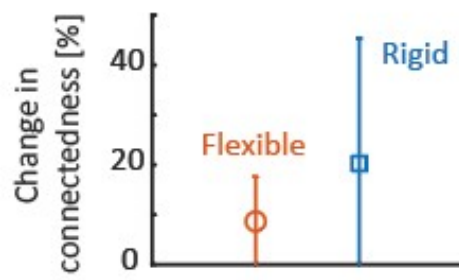


Fig. S18. Robotic blob connectedness Change in the number of robots in contact with each other, at the beginning and at the end of the experiments. For the rigid case shown in Fig.6C (n=11 trials, blue) and flexible case shown in Fig.6D (n=17 trials, red).

35 **References**

- 36
- 37 1. M Tennenbaum, Z Liu, D Hu, A Fernandez-Nieves, Mechanics of fire ant aggregations. *Nat. materials* **15**,
54–59 (2016).

38
39
40
41
42

43
44
45

46
47
48
49

50
51
52

53
54

55
56
57